

See discussions, stats, and author profiles for this publication at: <https://www.researchgate.net/publication/346416029>

The Rapid Intensification of Hurricane Michael (2018): Storm Structure and the Relationship to Environmental and Air–Sea Interactions

Article in *Monthly Weather Review* · October 2020

DOI: 10.1175/MWR-D-20-0145.1

CITATIONS

36

READS

320

5 authors, including:



Joshua Wadler

Embry-Riddle Aeronautical University

13 PUBLICATIONS 244 CITATIONS

[SEE PROFILE](#)



Jun A. Zhang

University of Miami

200 PUBLICATIONS 7,350 CITATIONS

[SEE PROFILE](#)



Robert F Rogers

Drexel University

69 PUBLICATIONS 2,034 CITATIONS

[SEE PROFILE](#)



Lynn K. Shay

University of Miami

163 PUBLICATIONS 7,471 CITATIONS

[SEE PROFILE](#)

The Rapid Intensification of Hurricane Michael (2018): Storm Structure and the Relationship to Environmental and Air–Sea Interactions

JOSHUA B. WADLER,^{a,b} JUN A. ZHANG,^{a,b} ROBERT F. ROGERS,^a BENJAMIN JAIMES,^c AND LYNN K. SHAY^c

^a NOAA/Atlantic Oceanographic and Meteorological Laboratory/Hurricane Research Division, Miami, Florida

^b Cooperative Institute for Marine and Atmospheric Studies, University of Miami, Miami, Florida

^c Rosenstiel School of Marine and Atmospheric Sciences, University of Miami, Miami, Florida

(Manuscript received 11 May 2020, in final form 14 October 2020)

ABSTRACT: The spatial and temporal variation in multiscale structures during the rapid intensification of Hurricane Michael (2018) are explored using a coupled atmospheric–oceanic dataset obtained from NOAA WP-3D and G-IV aircraft missions. During Michael's early life cycle, the importance of ocean structure is studied to explore how the storm intensified despite experiencing moderate vertical shear. Michael maintained a fairly symmetric precipitation distribution and resisted lateral mixing of dry environmental air into the circulation upshear. The storm also interacted with an oceanic eddy field leading to cross-storm sea surface temperature (SST) gradients of $\sim 2.5^{\circ}\text{C}$. This led to the highest enthalpy fluxes occurring left of shear, favoring the sustainment of updrafts into the upshear quadrants and a quick recovery from low-entropy downdraft air. Later in the life cycle, Michael interacted with more uniform and higher SSTs that were greater than 28°C , while vertical shear imposed asymmetries in Michael's secondary circulation and distribution of entropy. Midlevel ($\sim 4\text{--}8\text{ km}$) outflow downshear, a feature characteristic of hurricanes in shear, transported high-entropy air from the eyewall region outward. This outflow created a cap that reduced entrainment across the boundary layer top, protecting it from dry midtropospheric air out to large radii (i.e., $>100\text{ km}$), and allowing for rapid energy increases from air–sea enthalpy fluxes. Upshear, low-level ($\sim 0.5\text{--}2\text{ km}$) outflow transported high-entropy air outward, which aided boundary layer recovery from low-entropy downdraft air. This study underscores the importance of simultaneously measuring atmospheric and oceanographic parameters to understand tropical cyclone structure during rapid intensification.

KEYWORDS: Dynamics; Storm environments; Tropical cyclones; Air-sea interaction; Hurricanes/typhoons; Thermodynamics

1. Introduction

Hurricane Michael of 2018 was the first category-5 hurricane to make landfall in the continental United States since Hurricane Andrew of 1992. Forming from a broad area of low pressure in the western Caribbean Sea, Michael brought catastrophic damage to the Florida panhandle after it underwent rapid intensification (RI; greater than 30 kt ($1\text{ kt} \approx 0.51\text{ m s}^{-1}$) increase in intensity over 24 h) between 8 and 10 October in the Gulf of Mexico. During this time a field experiment was conducted where, for the first time, the simultaneous evolution of atmospheric and oceanographic parameters was measured during RI from a category-1 to a category-5 storm. This case study examines how Michael was influenced by nearby dry air and the complex oceanic thermal regime in the Gulf of Mexico during the initial stages of RI, and presents a hypothesis for how the asymmetric storm-relative environmental flow helped to sustain a warm and moist inflow layer as the storm became a major hurricane.

Forecasting tropical cyclone (TC) RI is one of the most important, yet difficult, challenges in the TC community due to the multiscale interactions that control structural and intensity changes (e.g., Marks and Shay 1998; Rogers et al. 2006, 2013a). Many of the complex atmospheric interactions stem from how a TC responds to deep layer environmental vertical wind

shear, often defined as the difference in environmental winds between 850 and 200 mb (hereafter referred to as shear) ($1\text{ mb} = 1\text{ hPa}$). Early studies of the response of TCs to vertical shear examined their response in a simplified framework. In a dry barotropic vortex exposed to shear, a low (high) potential temperature anomaly forms in the downtilt (uptilt) direction, which is balanced by a wavenumber-1 variation in vertical velocity (shifted 90° from the temperature anomalies) due to tilted isentropes (Jones 1995). In real TCs, the downtilt direction tends to be downshear to downshear-left (DSL; Reasor et al. 2004), making the DSL quadrant favorable for the precipitation maximum and the downshear-right (DSR) quadrant favorable for convective initiation (Reasor et al. 2013; DeHart et al. 2014) due to the convergence of low-level vorticity in a region of high θ_e values (Riemer 2016).

A great deal of research has been conducted in recent years focusing on characteristics of vertical velocity and precipitation structure in a shear-relative framework. Much of this work has explored differences in these structures for intensifying versus nonintensifying TCs, focusing on differences in the distribution and structure of deep convection upshear (i.e., convective bursts; Rogers et al. 2013b, 2015, 2016; Stevenson et al. 2014, 2018; Zagrodnik and Jiang 2014; Chen and Gopalakrishnan 2015; Rios-Berrios et al. 2016a,b; Rios-Berrios and Torn 2017; Wadler et al. 2018a; Leighton et al. 2018; Zhang and Rogers 2019) and the degree of symmetry in both stratiform precipitation and shallow convection (e.g., Jiang 2012; Kieper and Jiang 2012; Zagrodnik and Jiang 2014; Alvey et al. 2015;

Corresponding author: Joshua B. Wadler, joshua.wadler@noaa.gov

Tao and Jiang 2015; Tao et al. 2017; Jiang et al. 2018). The association between deep convection and stratiform precipitation upshear with TC intensification may be a manifestation of favorable thermodynamic conditions in that region. Zawislak et al. (2016) showed that in Hurricane Edouard (2014), persistent precipitation propagation into the upshear quadrants was associated with increases in midlevel humidity. The midlevel moistening tends to occur when hydrometeors from stratiform precipitation and anvil clouds in the DSL quadrant evaporate and sublimate before advecting into the upshear quadrants (Alvey et al. 2020).

TC intensification is also associated with favorable air-sea interactions, which can be complex when a storm interacts with oceanographic thermal gradients. Sea surface temperature (SST) cooling from upwelling leads to lower enthalpy fluxes and a stable atmospheric boundary layer (e.g., Chen et al. 2013; Lee and Chen 2014; Cione et al. 2013; Cione 2015), while the enthalpy fluxes are enhanced when a storm interacts with warm oceanic eddies (e.g., Shay et al. 2000; Hong et al. 2000; Lin et al. 2005, 2008; Jaimes and Shay 2009; Jaimes et al. 2015; Halliwell et al. 2015). The upper-ocean thermal structure can also be modified by interactions between background currents and the upwelling response (e.g., Jacob et al. 2000; Jaimes and Shay 2009, 2015; Halliwell et al. 2011; Yablonsky and Ginis 2013), and by barrier layers, which limit turbulent mixing of cool water into the mixed layer (e.g., Rudzin et al. 2017, 2018, 2019; Hlywiak and Nolan 2019; Balaguru et al. 2020). While the interaction between a TC and oceanographic thermal gradients leads to regions of enhanced and suppressed enthalpy fluxes, what remains unclear is how the oceanographic thermal gradients (and their orientation relative to the storm) influence TC intensification and the shear-relative asymmetries in vertical motion and precipitation. The first part of this study examines how the structure of Hurricane Michael during the early stages of RI was related to its interaction with midlevel dry air and oceanographic thermal gradients in the Gulf of Mexico.

In mature hurricanes, Riemer et al. (2010, 2013) showed, using idealized numerical simulations, that quasi-persistent downdrafts in the left-of-shear quadrants transport low- θ_e air to the boundary layer. Several observational studies have analyzed the role of downdrafts at different storm-relative locations and points in the TC life cycle (Barnes et al. 1983; Powell 1990; Barnes and Powell 1995; Didlake and Houze 2009, 2013; Cione et al. 2000, 2013; Eastin et al. 2012; Barnes and Dolling 2013; Molinari et al. 2013; Dolling and Barnes 2014; Zhang et al. 2017; Nguyen et al. 2017, 2019) and generally concur that downdrafts create unfavorable thermodynamic conditions in the boundary layer, particularly in the upshear quadrants. While the boundary layer has a chance to recover via the air-sea enthalpy fluxes before the air enters the eyewall (Molinari et al. 2013; Zhang et al. 2017; Wadler et al. 2018b), the effects of downdrafts can also be negated if the midtropospheric air transported into the boundary layer already has high θ_e values (Barnes and Powell 1995; Wroe and Barnes 2003; Barnes 2008; Wadler et al. 2018b).

Multiple processes can lead to changes in midlevel θ_e values. High- θ_e air from the boundary layer can be transported to the

middle troposphere through convective updrafts (e.g., Barnes et al. 1983; Powell 1990; Barnes and Powell 1995), while midtropospheric θ_e values can be reduced by lateral mixing of dry environmental air into the TC circulation (e.g., Tang and Emanuel 2010, 2012; Zawislak et al. 2016; Nguyen et al. 2017; Alland et al. 2017). Another process that could influence midtropospheric θ_e values is large-scale advection by an asymmetric secondary circulation, which exists as a response to shear as identified by both balance models and observational composites (e.g., Jones 1995; Reasor et al. 2013; Zhang et al. 2013; DeHart et al. 2014). Generally, the downshear quadrants are characterized by deep (\sim 1.5–2 km altitude) inflow layers with outflow above; the upshear quadrants are characterized by low-level (\sim 0.5–2 km altitude) outflow layers with inflow above (Zhang et al. 2013; Reasor et al. 2013). How the asymmetric secondary circulation relates to the distribution of entropy remains unknown.

With an emphasis on these two stages of Hurricane Michael's rapid intensification, the overall objectives of the paper are to:

- 1) Address how the precipitation and convective distribution in Hurricane Michael was influenced by both environmental wind shear and oceanic thermal gradients during Michael's early life cycle, when it was a category-1–2 hurricane;
- 2) Investigate how the asymmetric secondary circulation, once Michael became a major hurricane, influenced the distribution of midlevel and boundary layer θ_e as well as the effects of downdrafts;
- 3) Discuss how the kinematic and thermodynamic structural asymmetries related to processes described in objectives 1 and 2 potentially impacted Michael's rapid intensification.

2. Data and methodology

From 8 to 10 October 2018, four NOAA WP-3D (P-3) and three NOAA G-IV aircraft missions observed the RI of Hurricane Michael (Table 1). The sampling began as the storm center passed west of Cuba as a category-1 hurricane and extended until right before landfall as a category-5 hurricane (Fig. 1a). The G-IV (with a flight altitude of 40 000–45 000 ft; \sim 12.2–13.7 km) sampled the environment surrounding the storm with dropsondes while the P-3 (with a flight altitude of 8000–10 000 ft; \sim 2.4–3 km) sampled the inner core with airborne pseudo-dual-Doppler radar, dropsondes, and ocean expendables. The flight pattern for each G-IV mission included a quasi-circumnavigation with a radius ranging between 100 and 200 km with respect to the TC center, allowing us to explore the azimuthal distribution of midlevel θ_e close to the inner core. Throughout this manuscript, mission IDs are used to refer to specific flights. They are typically given by “year-month-day-plane ID-mission number for that day,” where “H” and “N” are the P-3 and G-IV plane IDs, respectively. Since all the missions occurred over a 2-day period, the mission IDs are abbreviated by “day-plane ID-mission number” (e.g., 20181008H1 is referred to as 08H1 and 201809N2 is referred to as 09N2).

TABLE 1. A list of the number of dropsondes and ocean expendables (AXBTs, AXCPs, and AXCTDs) released during the four P-3 missions and three G-IV missions into Michael. On-station times are the times of the first and last dropsondes released during the mission.

Flight ID (abbreviation)	On-station time	No. of dropsondes	No. of ocean expendables (AXBT, AXCP, AXCTD) released (successful)
20181008H1 (08H1)	2256 UTC 8 Oct–0138 UTC 9 Oct	19	19 (14), 8 (5), 3(3)
20181009H1 (09H1)	0838–1444 UTC 9 Oct	31	16 (9), 6 (2), 2 (2)
20181009H2 (09H2)	2101 UTC 9 Oct–0412 UTC 10 Oct	29	19 (15), 0 (0), 0 (0)
20181010H1 (10H1)	0923–1411 UTC 10 Oct	25	19 (7), 4 (0), 1 (1)
20181008N1 (08N1)	1756 UTC 8 Oct–0108 UTC 9 Oct	38	—
20181009N1 (09N1)	0552–1213 UTC 9 Oct	36	—
20181009N2 (09N2)	1755–2215 UTC 9 Oct	27	—

a. Dropsondes

Dropsondes measure a single profile of temperature, humidity, wind speed, and wind direction with a $\sim 7\text{ m}$ vertical resolution (Hock and Franklin 1999) as they fall from the aircraft to the sea surface. In each P-3 mission, dropsondes were released along radial legs at endpoints, midpoints, and center points. Occasionally, they were released into the eyewall near the radius of maximum wind speed (RMW) for estimates of storm intensity. Dropsondes released from the G-IV generally sampled the environment surrounding the storm. The number of dropsondes released during each P-3 and G-IV mission is given in Table 1.

Each dropsonde is postprocessed using NCAR's ASPEN software and put into storm-relative coordinates. The storm center is determined by the 2-min-resolution track data (available at https://www.aoml.noaa.gov/hrd/Storm_pages/michael2018/track.html) based on aircraft fixes following the method of Willoughby and Chelmow (1982). The dropsondes are interpolated every 10 m from 10 m up to 3.0 km (14.0 km) altitude for ones released by the P-3 (G-IV). After postprocessing, some dropsondes from the P-3 were missing 10 m quantities (28 out of 104). To rectify this, we applied a linear best fit to data within the lowest 100 m to determine the 10 m value (same methodology as Wadler et al. 2018b). The 10 m air temperature and humidity are combined with the SST data (section 2c) to calculate sensible heat and latent heat flux [Eqs. (1) and (2) respectively; combined referred to as enthalpy flux]:

$$Q_s = \rho_a c_p C_h U_{10} (\text{SST} - T_{10}), \quad (1)$$

$$Q_l = \rho_a L_v C_e U_{10} (q_s - q_{10}), \quad (2)$$

where ρ_a is the density of dry air; $C_h = C_e = 1.1 \times 10^{-3}$ are the exchange coefficients for sensible heat and latent heat fluxes, respectively [values derived from Zhang et al. (2008)]; $c_p = 1004 \text{ J kg}^{-1} \text{ K}^{-1}$ is the specific heat of dry air at constant pressure; $L_v = 2.5 \times 10^6 \text{ J kg}^{-1}$ is the latent heat of evaporation; T_{10} and SST are the 10 m air and sea surface temperature, respectively; and q_{10} and q_s are the 10 m and sea surface specific humidity, respectively.

Horizontal contour plots are used to evaluate the distribution of both environmental and in-storm thermodynamics. Following the methodology in Wadler et al. (2018b), dropsonde-measured variables in all horizontal contour plots are interpolated using a natural neighbor scheme (which

preserves dropsonde measured values) with the storm-relative position of the dropsondes at that altitude overlaid. While the sparse dropsonde sampling certainly does not resolve all gradients within and around the TC, the gradients within the contour plots represents the minimum gradients present over the sampled area (i.e., actual gradients can only be larger than

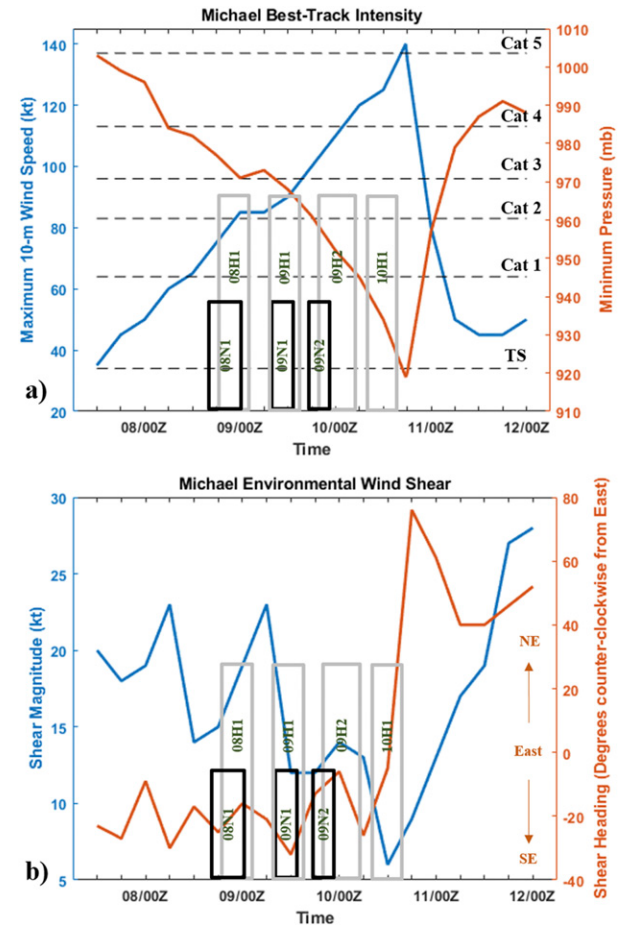


FIG. 1. Time series of Michael's (a) best track intensity and minimum central pressure and (b) environmental wind shear magnitude and direction obtained from the SHIPS database. In both panels, the approximate times of the three G-IV missions (black boxes) and four P-3 missions (gray boxes) are overlaid.

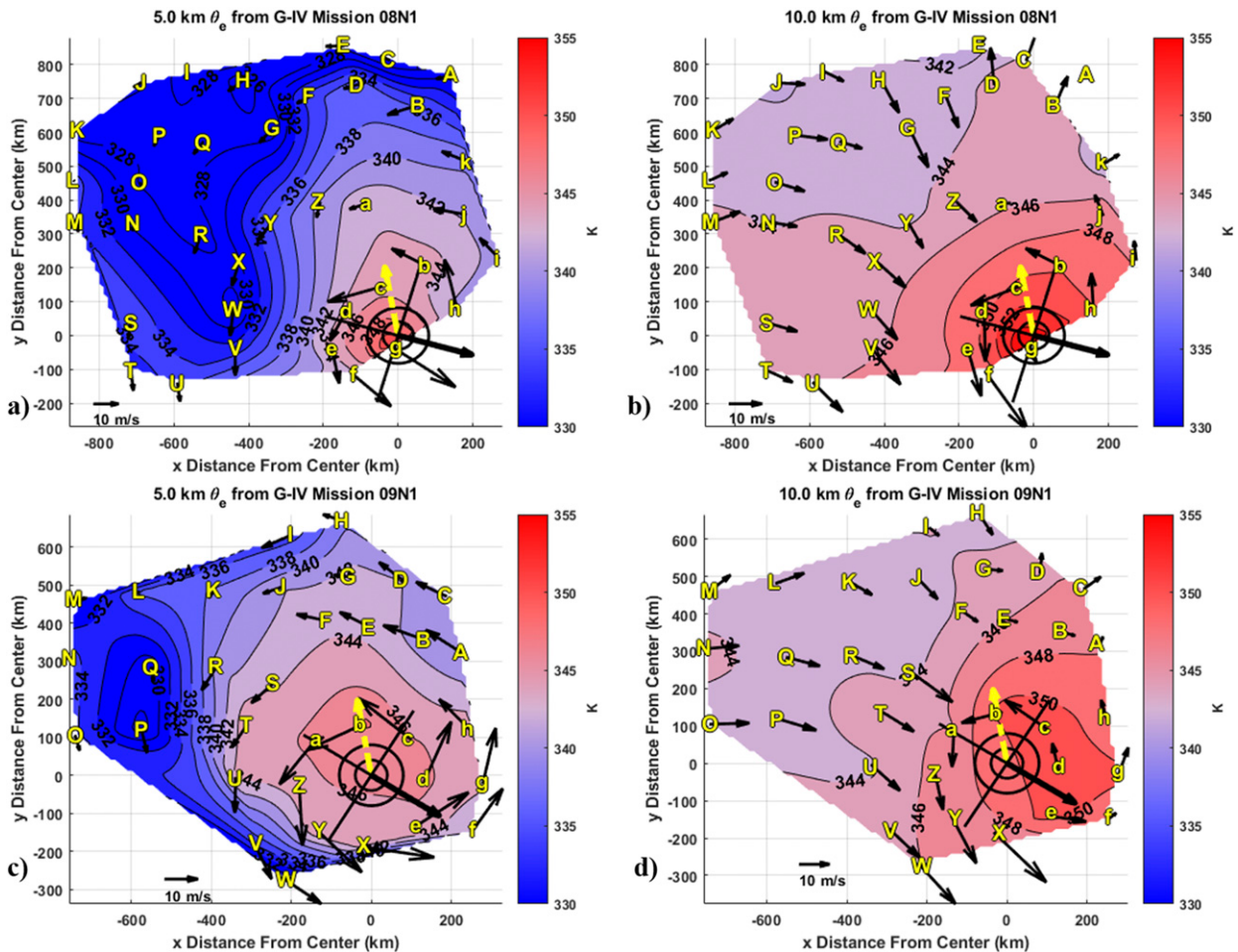


FIG. 2. Equivalent potential temperature (θ_e) at (a) 5.0 and (b) 10.0 km from dropsondes released during G-IV mission 08N1. (c),(d) As in (a) and (b), but for the 09N1 mission. In each panel, the contour interval is 2 K and dropsondes are labeled by letter in the order that they are launched (all capital letters followed by lowercase letters). Storm-relative wind vectors derived from the dropsondes at the respective heights are overlaid. The black range rings represent the RMW and $2 \times$ RMW at 2 km altitude from the closest in-time P-3 mission. The solid black (dashed yellow) arrow from the center represents the shear (motion) vector. Solid black lines from the storm center outline the shear-relative quadrants.

those shown in the contour plots). In the contour plots for the P-3 missions shown in section 3, only dropsondes released during the standard flight pattern (figure-4 or butterfly) are included. That is, if the plane returned to an area to perform a research module (often multiple hours later), those dropsondes were not included because they can add artificial gradients by sampling transient features.

b. P-3 tail Doppler radar

On all four P-3 missions, X-band tail Doppler radar data were collected. A variational algorithm is used to postprocess the raw data (Gamache 1997), which solves the Doppler projection and continuity equations to project the data onto a grid with a 2.0 km horizontal resolution and a 0.5 km vertical resolution (Reasor et al. 2009). The analyses for each mission are broken down into swaths, defined as a radial penetration (inbound/outbound from the center) and a downwind leg, which are commonly used to analyze convective and mesoscale

processes (e.g., Rogers et al. 2013b, 2015, 2016; Reasor et al. 2013; Fischer et al. 2020).

At multiple locations, radial cross sections are taken through radar swaths at the dropsonde splash locations to compare the thermodynamic profiles from the dropsondes with broader kinematic characteristics observed from the Doppler radar. The cross sections are only taken at the splash location for dropsondes released by the P-3 and each one is averaged 4 km upwind and downwind to maximize data coverage. While there is uncertainty in comparing collocated data from two independent measurement platforms, the radar sweeps from the P-3 sample nearly simultaneously with the dropsonde release (though it takes \sim 3–4 min for a dropsonde from the P-3 to splash). As in Wadler et al. (2018b), the wind speeds measured from the dropsondes are compared to the wind speeds derived from radar swaths at the same storm-relative locations and radar vertical levels (i.e., every 0.5 km from 0.5 km altitude up to 3.0 km). The root-mean-square-difference in the wind

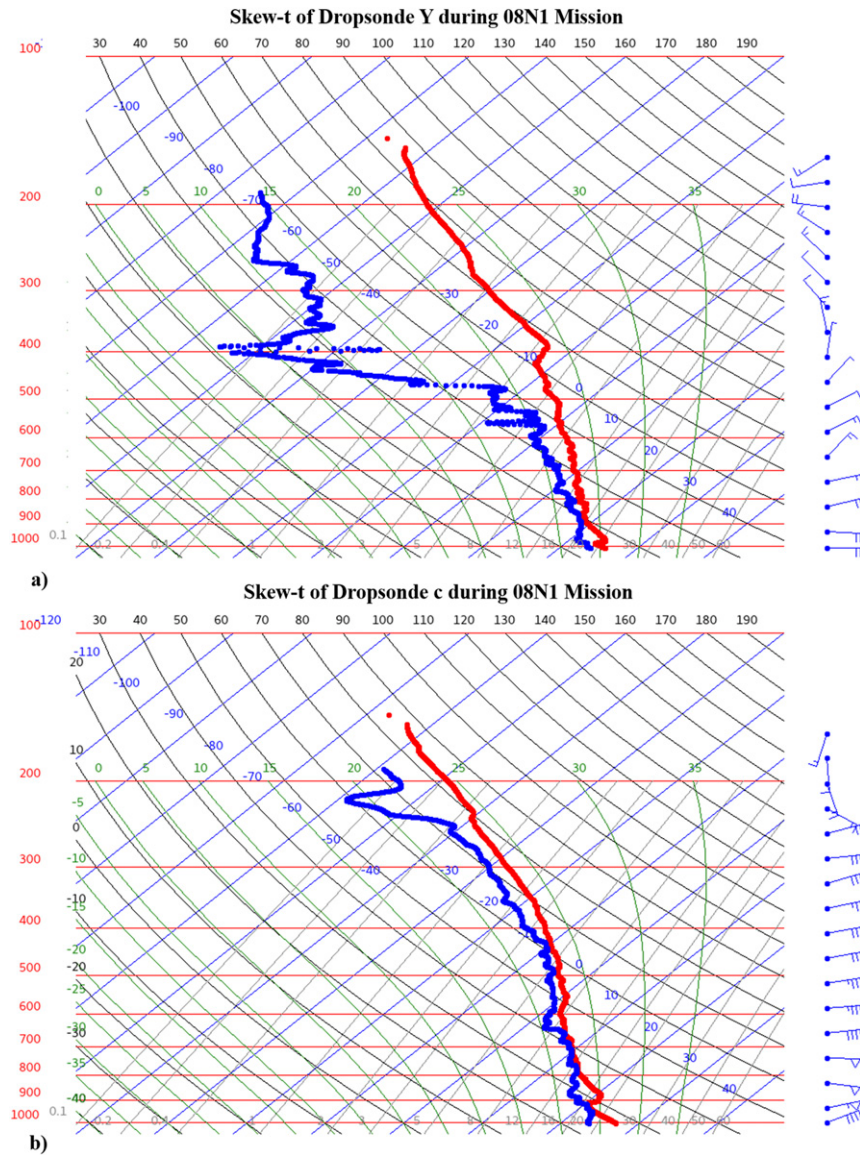


FIG. 3. A skew T -log of (a) dropsonde Y (released 2246 UTC 8 Oct) and (b) dropsonde c (released 2336 UTC 8 Oct) from the 08N1 G-IV mission.

speeds measured between both platforms is 4.98 m s^{-1} , a reasonable comparison that is similar to other studies comparing measurements from multiple platforms (e.g., Reasor et al. 2009; Rogers et al. 2012; Klotz and Uhlhorn 2014) and yields confidence that the dropsondes and radar analyses are sampling the same kinematic features.

In each mission, all radar swaths are averaged together to create a merged analysis, which is useful for diagnosing vortex-scale characteristics, but mask convective and mesoscale variations where multiple swaths overlap (e.g., the inner core). In this study the merged analyses are used to diagnose vortex tilt (defined as the difference in location of minimum tangential wind speed between 2.0 and 8.0 km in the radar-merged analysis).

TABLE 2. A summary of the vortex tilt during each of the P-3 flight, determined as the difference in location of minimum tangential wind speed between 2.0 and 8.0 km in the radar-merged analysis. For comparison, the environmental shear direction from SHIPS is also given.

	08H1	09H1	09H2	10H1
2–8 km tilt direction (degrees counterclockwise from east)	326.3	0	26.6	225
SHIPS 850–200 mb shear heading (degrees counterclockwise from east)	344	328	354	0
2–8 km tilt magnitude (km)	7.2	6.0	4.5	2.8

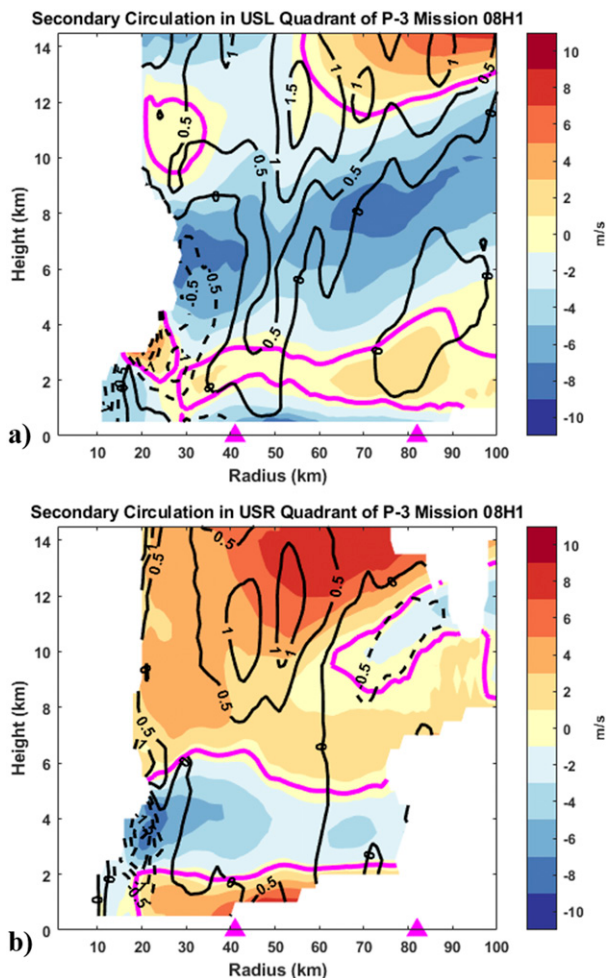


FIG. 4. Quadrant-averaged radial wind (shaded; magenta line outlines zero contour) and vertical velocity (black contoured; solid = positive and dashed = negative) in the (a) upshear-left quadrant and (b) upshear-right quadrant during the 08H1 P-3 mission. Pink triangles on the abscissa represent the RMW and $2 \times$ RMW at 2 km altitude. Each panel requires 40% data coverage.

wind speed between 2.0 and 8.0 km altitude) and to create quadrant-averaged radar analyses, since individual swaths generally do not contain enough azimuthal coverage to diagnose vortex-scale characteristics.

c. Ocean expendables

Ocean thermal and current measurements were taken from a variety of airborne expendable bathythermographs (AXBTs), conductivity-temperature-depth sensors (AXCTDs), and current profilers (AXCPs). To maximize our ability to calculate accurate air-sea enthalpy fluxes, the oceanic profilers were released simultaneously with nearly all dropsondes on each P-3 mission (numbers given in Table 1). During the 08H1 mission, extra ocean expendables were released ahead of the storm to obtain prestorm measurements. The accuracy of the thermistor in these instruments is $\pm 0.1^\circ\text{C}$ for the AXCTD (Johnson 1995) and $\pm 0.2^\circ\text{C}$ in the AXCP and AXBT (Boyd 1987).

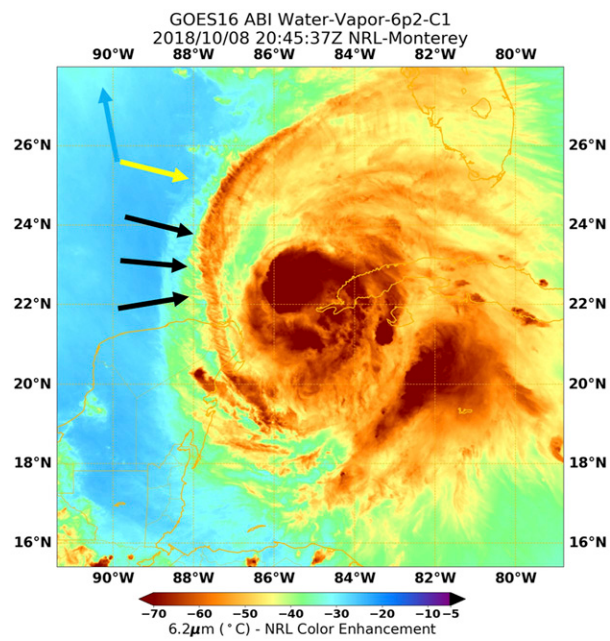


FIG. 5. Water vapor imagery centered on Hurricane Michael from GOES-16 at 2045 UTC 8 Oct. Motion (blue) and vertical shear (yellow) vectors are overlaid. Black arrows outline an upper-level upshear arc-shaped cloud structure. Image was obtained from <https://www.nrlmry.navy.mil/TC.html>.

A further description of the error characteristics of these instruments can be found in Shay et al. (2011). In the present study, the ocean expendables are used to obtain measurements of SST and ocean heat content (OHC) relative to the 26°C isotherm.

Since the overall success rate of the ocean expendables was 68%, some of the dropsondes are not collocated with a SST measurement for enthalpy flux calculations. To rectify this, the SST measurements during each mission were interpolated to missing points using a Laplacian interpolation method based on Hankin et al. (2006). This method, which was used by Jaimes et al. (2015) and Rudzin et al. (2017) for interpolating irregular oceanographic measurements in hurricanes, allowed us to obtain SST measurements that are consistent with observed oceanic thermal variability at locations where the oceanic profiler failed. Since this Laplacian interpolation method was unable to get interpolated values at some isolated dropsonde points that were away from the main data cluster (i.e., end points), we followed the methodology given by Jaimes and Shay (2010), which uses a Gaussian weighted average based on all available measurements within a radius of 1° to get an interpolated value.¹ In Jaimes et al. (2015), the mapping error associated with the interpolation techniques was negligible as the overall temperature bias between actual and interpolated SSTs (compared at data points) is -0.03°C

¹ Given the added uncertainty of using the Gaussian-weighted average, those locations are noted in Figs. 8 and 10.

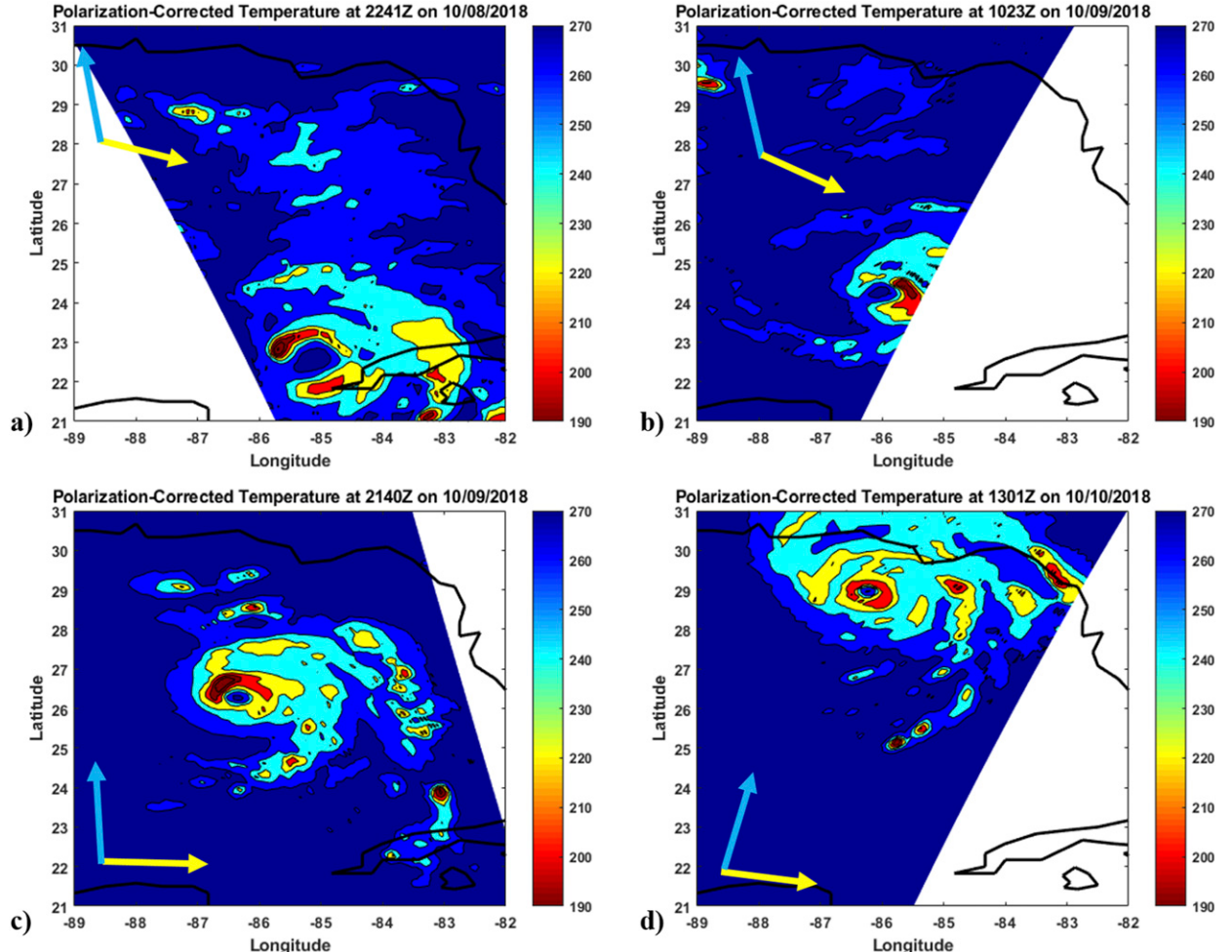


FIG. 6. Polarization-corrected temperature (PCT) calculated for the 85–91 GHz data obtained from the Special Sensor Microwave Imager/Sounder (SSMI/S) satellites following the method in Cecil and Chronis (2018) at (a) 2241 UTC 8 Oct, (b) 1023 UTC 9 Oct, (c) 2140 UTC 9 Oct, and (d) 1301 UTC 10 Oct. Motion (blue) and vertical shear (yellow) vectors are overlaid in each panel. Data were obtained from <https://earthdata.nasa.gov/>.

with a standard deviation of 0.29°C and a correlation coefficient of 0.99.

3. Results

Hurricane Michael's intensity evolution from the National Hurricane Center (NHC) best track data, along with the times of the aircraft missions, is given in Fig. 1a. Between the approximate start of NOAA aircraft sampling at 0000 UTC 9 October and the time Michael made landfall at around 1730 UTC 10 October, the storm underwent RI and strengthened from 75 to 140 kt, with its greatest increase in intensity occurring right before landfall. The 850–200 mb environmental wind shear, obtained from the Statistical Hurricane Intensity Prediction Scheme (SHIPs; DeMaria and Kaplan 1999) database (Fig. 1b), remained between 18 and 23 kt during the first two P-3 missions, but then decreased to less than 10 kt right before landfall. Throughout all missions, the shear direction was consistently toward the ESE direction, controlling for

possible changes in storm structure due to varying shear direction (Cione et al. 2013; Onderlinde and Nolan 2017).

a. Early intensification stage

1) STORM STRUCTURE AND INTERACTION WITH ENVIRONMENT

During the first two sampling periods there is low- θ_e [calculated using the method of Bolton (1980)] air to the north and west of Michael at 5.0 km (Figs. 2a,c) and 10.0 km altitude (Figs. 2b,d; the highest altitude with consistent dropsonde coverage). The thermodynamically unfavorable air is likely associated with an upper-level trough, the same source of environmental shear on the storm (Beven et al. 2019). As evident from dropsonde Y from the 08N1 mission (Fig. 3a), the low θ_e is due to dry air above 500 mb (~ 5800 m), a signature generally consistent through dropsondes V–Z, though the thickness of the dry air layer does vary (not shown). The upper-level dry air is accompanied by storm-relative winds between 5 and 15 kt moving toward the storm (Fig. 2b).

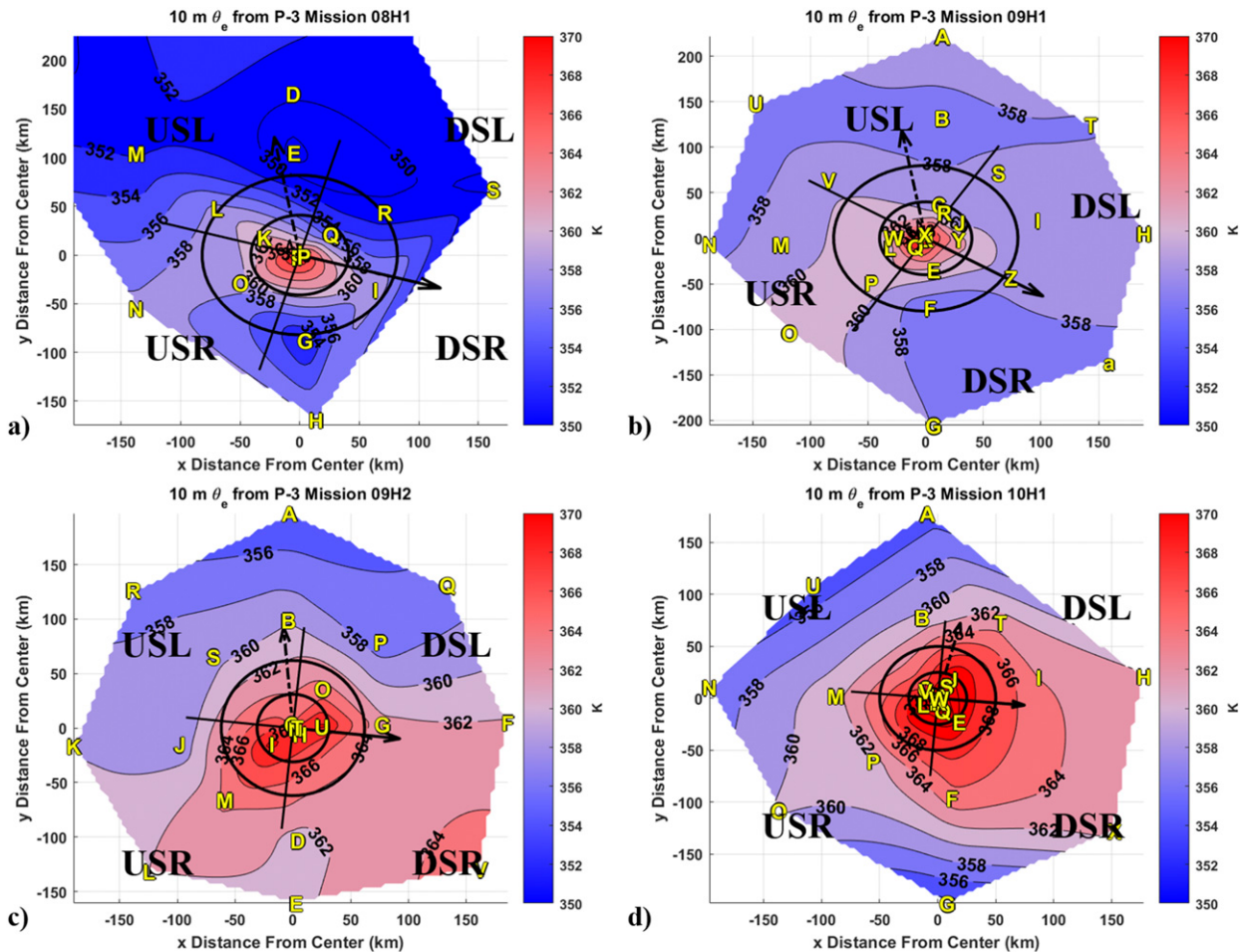


FIG. 7. Equivalent potential temperature (θ_e) at 10 m from dropsondes released during P-3 missions (a) 08H1, (b) 09H1, (c) 09H2, and (d) 10H1. In each panel, dropsondes are labeled by letter in the order that they are launched (all capital letters followed by lowercase letters). The contour interval for all panels is 2 K. The black range rings represent the 2-km RMW and $2 \times$ RMW from the radar-merged analysis for the given mission. The solid (dashed) black arrow from the center represents the shear (motion) vector.

Despite a wind shear magnitude of 15–20 kt during the first mission, there is a relatively small 7.2 km vortex tilt toward the east-southeast during the 08H1 mission (Table 2; close in time to the 08N1 mission). The storm-relative flow at 5.0 and 10.0 km altitude reveals a closed circulation from dropsondes at \sim 200 km radius and similar θ_e values at all of the azimuths that were observed (Figs. 2a,b). This is likely a reflection of weak storm-relative environmental flow relative to the strength of the inner-core swirling winds, which can help limit dry air entrainment into the circulation (Riemer and Montgomery 2011). The profile from Dropsonde c, released in the upshear-left (USL) quadrant during the \sim 200 km radius circumnavigation period of the 08N1 mission (Fig. 3b), is nearly saturated below 250 mb, indicating that the dry upper-level air at \sim 400 km radius does not significantly entrain into the circulation. Dropsondes d–f have similar characteristics, though they have a dry layer between 300 and 400 mb (not shown). The dry layer above 250 mb in Dropsonde c likely reflects sublimational cooling below the anvil cloud (as discussed in Alvey et al. 2020) and in the descending inflow layer

between 4 and 10 km altitude of the USL quadrant. This inflow layer is noticed through the quadrant-averaged radar analysis during the 08H1 mission [Fig. 4a; similar to what was noticed in Didlake et al. (2018) and Dai et al. (2019)].

The favorable TC–environmental interactions during this sampling period are also noticed in the upper-levels. The quadrant-averaged radial wind in the USL quadrant shows an outflow layer above 11 km altitude that extended from 60 km to past 100 km radius (Fig. 4a). The outflow layer began at 6 km altitude in the upshear-right (USR) quadrant and extended outward from the eyewall (Fig. 4b). Beven et al. (2019) suggested that the outflow was likely enhanced (throughout all the missions) by upper-level difffluence caused by the shortwave trough to the west of Michael. The water vapor imagery taken during the 08N1 mission indicates an arc-shaped cloud structure was present in the upshear outflow layer (Fig. 5), which is a feature associated with RI (Ryglicki et al. 2018a,b, 2019) because can signify a reduction of local shear that is potentially responsible for the small vortex tilt. Likely as a result, the PCT imagery (Fig. 6a) reveals nearly complete azimuthal coverage

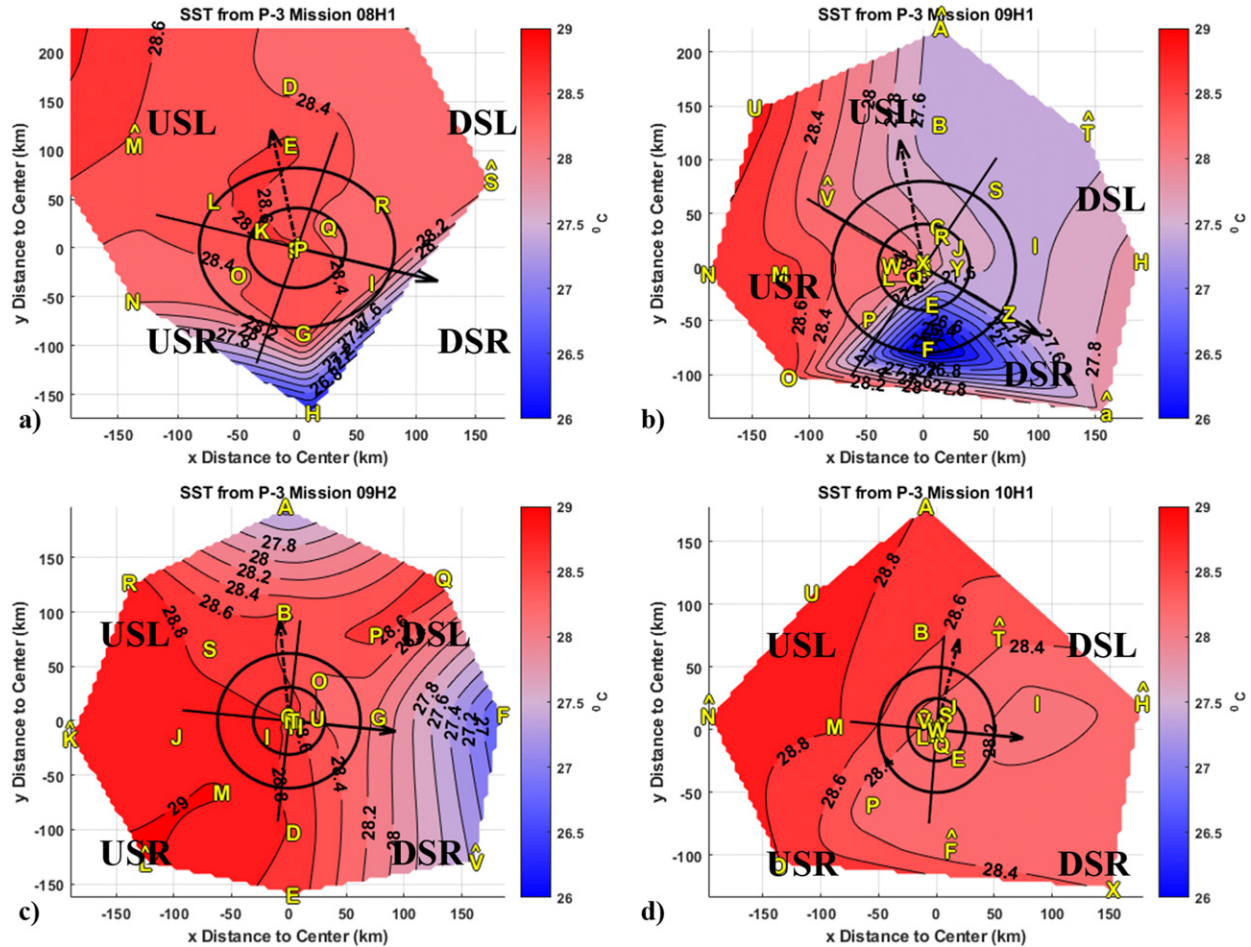


FIG. 8. Sea surface temperature during P-3 missions (a) 08H1, (b) 09H1, (c) 09H2, and (d) 10H1. Dropsondes locations at 10 m are labeled by letter in the order that they are launched (all capital letters followed by lowercase letters). Locations where the SSTs are extrapolated using the Gaussian-weighted average are labeled with a yellow hat (\wedge) above the letter. The contour interval for all panels is 0.2°C . The black range rings represent the 2-km RMW and $2 \times$ RMW from the radar-merged analysis for the given mission. The solid (dashed) black arrow from the center represents the shear (motion) vector.

of weaker ice scattering (PCTs $\sim 250\text{--}260\text{ K}$) around much of the eyewall with deep convective cores on both the northwest (USL) and southeast (DSR) sides.

During the following 09N1 mission, the fairly symmetric midlevel θ_e values within the innermost 200 km (Figs. 2c,d) and marginal 6.0 km vortex tilt (Table 2) signify continued resistance to entrainment of dry environmental air. The PCT imagery during the approximate time of the 09N1 mission shows that the western and southwestern part (upshear to upshear-right) of the eyewall remained free of deep convection (Fig. 6b). The strongest convection was on the eastern side of the storm (downshear to downshear-left), collocated with the highest environmental θ_e values (Figs. 2c,d).

2) INFLUENCE OF BOUNDARY LAYER THERMODYNAMIC VARIABILITY AND AIR-SEA INTERACTIONS

In addition to favorable TC-environmental interactions, the development and sustainment of inner-core convection depends on high- θ_e air entering the eyewall from the boundary

layer (i.e., [Malkus and Riehl 1960; Emanuel 1986](#)). During the 08H1 mission, when Michael had just entered the Gulf of Mexico, the largest 10 m θ_e was in the USL quadrant, followed by the DSR quadrant (Fig. 7a). There were large radial gradients in θ_e , especially on the north side (DSL quadrant) where the θ_e difference between the storm center and $r^* = 2$ ($r^* = R/\text{RMW}_{2\text{km}}$) was $\sim 15\text{ K}$.

During this time the SST inside $r^* = 2$ was between 28.2° and 28.4°C , but decreased to 26.8°C at 150 km south of the center (Fig. 8a), indicative of a cold wake. The low- θ_e air in the DSL quadrant combined with a local maximum in wind speed (Fig. 9a) led to a maximum latent heat flux near the RMW of $\sim 650\text{ W m}^{-2}$ (Fig. 10a) and sensible heat flux of $\sim 120\text{ W m}^{-2}$ (Fig. 10b). Interestingly, the quadrant-averaged vertical velocity in the USL quadrant reveals that eyewall updrafts generally extended from the boundary layer (defined here as the height of the inflow layer, similar to [Zhang et al. 2011](#)) to 14 km altitude (Fig. 4a) and the microwave imagery reveals a deep convective core in the USL (northwest) quadrant (Fig. 6a).

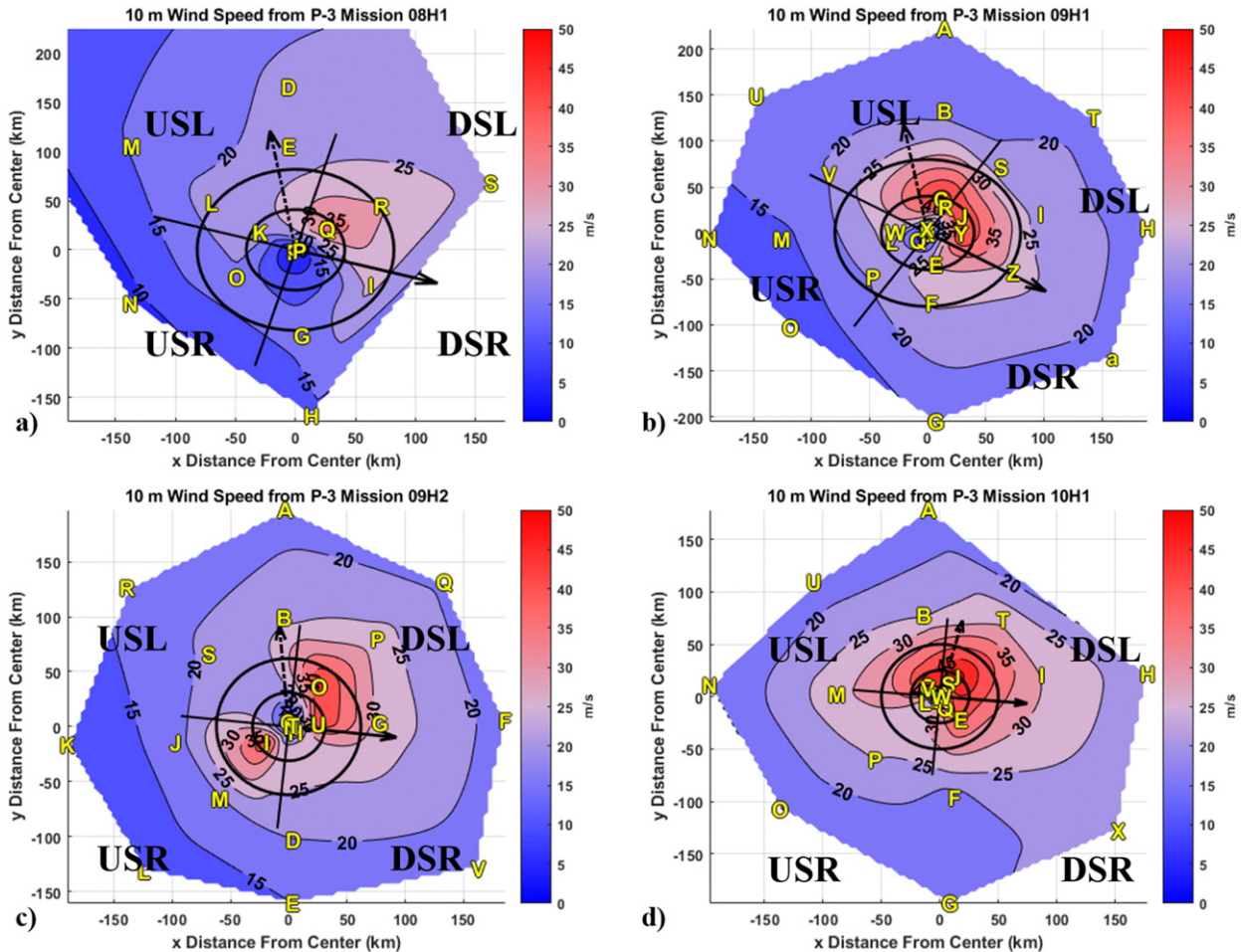


FIG. 9. As in Fig. 7, but for 10 m dropsonde-measured wind speed.

With the quadrant-averaged eyewall updrafts still coupled to the boundary layer, the combination of higher enthalpy fluxes in the DSL quadrant and already high- θ_e air near the RMW of the USL quadrant likely led to high-entropy air entering updrafts in the left-of-shear quadrants, directly leading to increased mid- to upper-level latent heating.

The quadrant-averaged radar cross section in the USL quadrant also reveals outflow between 2 and 4 km altitude that extended from radially inward of the RMW to eyewall updrafts near the low-level RMW (Fig. 4a). This indicates that that eyeyewall mixing occurred in the low levels of the USL quadrant, which is a mechanism to enhance eyewall θ_e and support upshear convection (Eastin et al. 2005a,b; Cram et al. 2007; Bell and Montgomery 2008; Barnes and Fuentes 2010; Dolling and Barnes 2012, 2014; Guimond et al. 2016; Hazelton et al. 2017). The presence of eye-eyewall mixing is supported by dropsonde K during the 08H1 mission (Fig. 7a), located radially inward of the RMW [similar to that discussed in Aberson et al. (2006)], whose wind measurements show storm relative outflow (maximized at ~ 1500 m) accompanied by an increase in θ_e with height from ~ 356 K at 1000 m to ~ 361 K at 1500 m (Fig. 11). While no dropsondes were released in the eyewall of the USR

quadrant, the quadrant-averaged radar cross section in this region also reveals storm-relative outflow below 2-km altitude and radially inward of the RMW (Fig. 4b).

While throughout all four P-3 missions the maximum 10 m θ_e in the eye remained at a similar magnitude (~ 370 – 375 K), the values increased significantly near the RMW. During the 09H1 mission the storm was interacting with a mesoscale cool oceanic eddy on the south (right of shear) side of the storm, creating a $\sim 2.5^\circ\text{C}$ gradient in SST (Fig. 8b) and a $\sim 40 \text{ kJ cm}^{-2}$ gradient in OHC (not shown) between $r^* = 2$ on the south side and north sides of the storm. The higher SSTs on the western side of the storm were associated with a mesoscale warm oceanic eddy ($\text{OHC} > 70 \text{ kJ cm}^{-2}$). TCs in the Gulf of Mexico typically move over mesoscale warm and cool eddies with warm (cool) eddies having typical diameters of 200–400 km (100–150 km) and vertical signatures of ~ 1000 m (~ 800 m) (Hamilton 1992; Zavala-Hidalgo et al. 2003). With warm (cool) eddies associated with suppressed (enhanced) SST cooling during TC passage (e.g., Shay et al. 2000; Jacob et al. 2000; Walker et al. 2003; Jaimes and Shay 2009), they can lead to significantly enhanced (suppressed) air-sea enthalpy fluxes (e.g., Jaimes et al. 2015, 2016).

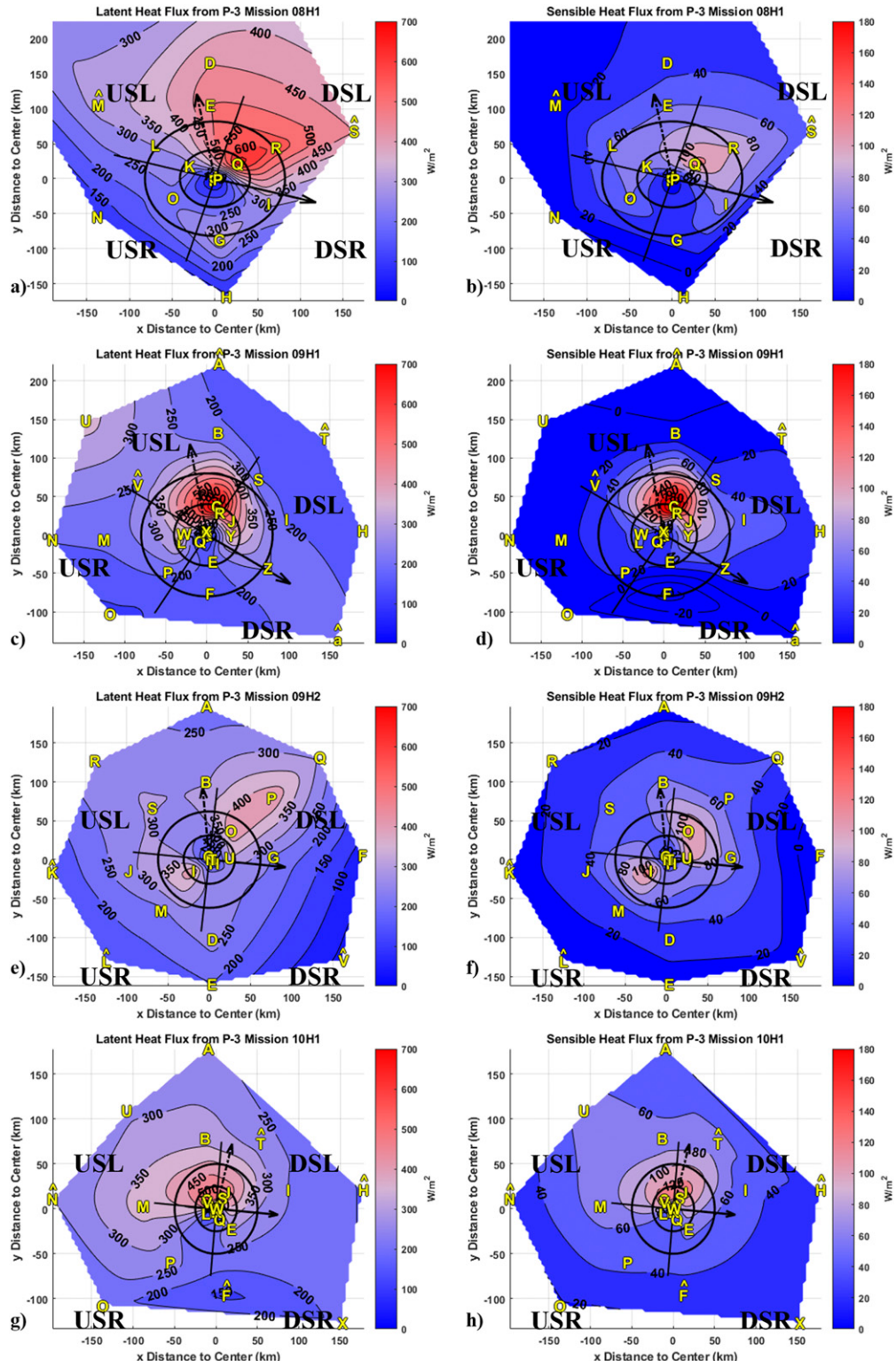


FIG. 10. (left) Latent heat flux during P-3 missions (a) 08H1, (c) 09H1, (e) 09H2, and (g) 10H1 and (right) sensible heat flux during P-3 missions (b) 08H1, (d) 09H1, (f) 09H2, and (h) 10H1. Dropsondes locations at 10 m are labeled by letter in the order that they are launched (all capital letters followed by lowercase letters). Locations where the SSTs are extrapolated using the Gaussian-weighted average are labeled with a yellow hat (^) above the letter. The contour intervals in (a), (c), (e), and (g) is 50 W m^{-2} while it is 20 W m^{-2} in (b), (d), (f), and (h). The black range rings represent the 2 km RMW and $2 \times$ RMW from the radar-merged analysis for the given mission. The solid (dashed) black arrow from the center represents the shear (motion) vector.

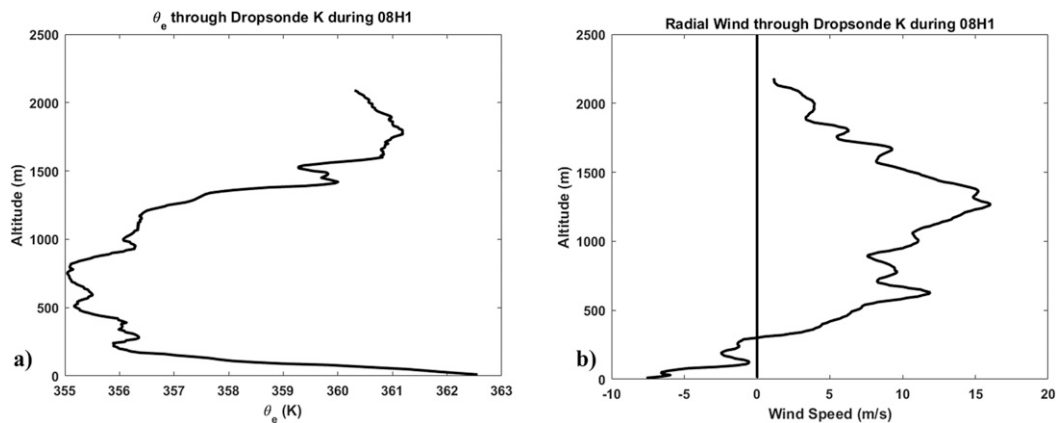


FIG. 11. Profile of (a) equivalent potential temperature and (b) radial velocity (negative = inflow, positive = outflow) from dropsonde K during the 08H1 mission. In (b) the zero line is drawn.

As with the 08H1 mission, the warmer waters, stronger wind speed (Fig. 9b) and large enthalpy fluxes (Figs. 10c,d) near the eyewall in the USL quadrant during the 09H1 mission were concurrent with eyewall convection propagating upshear (Figs. 6b and 12). The quadrant-averaged quantities also indicate that inner-core convective downdrafts were present in both the USL andUSR quadrants (Figs. 12a,c), likely transporting lower θ_e air from the midtroposphere to the boundary layer. Interestingly, even in the presence of cool waters, the radar analysis indicates that there were low and midlevel updrafts in the DSR quadrant (Fig. 12d), signifying that the boundary layer θ_e was recovered before air traversed from the upshear quadrants to that region.

With the DSR quadrant being the preferential location for convective initiation (e.g., DeHart et al. 2014), and a region characterized by tilt-induced mechanical ascent (e.g., Jones 1995), we hypothesize that the geometric relationship between the gradient separating the warm and cool oceanic eddies and the shear direction was preferential for boundary layer recovery and for Michael to intensify. That is, for intensification to occur, the most important location to have warm waters and large enthalpy fluxes is the left-of-shear quadrants because, when downdrafts form in this region, the thermodynamically unfavorable air they transport into the boundary layer has a $\sim 90^\circ$ spiral trajectory (95 km arc-length if traveling 90° in a purely angular trajectory at 60 km radius) to recover before reaching the relatively cool waters (similar conclusion to Nguyen et al. 2019). The cool (25.5°C) waters and low (200 W m^{-2}) total enthalpy flux near the eyewall of the DSR quadrant would not inhibit convective initiation because of the already high- θ_e air from enhanced enthalpy fluxes ($\sim 900 \text{ W m}^{-2}$) due to warm waters and larger wind speeds upwind. Additionally, if eyewall updrafts are still coupled to the boundary layer as they rotate upshear, a region typically characterized by tilt-induced mechanical descent, the large enthalpy fluxes can help sustain them into that region.

The significance of changes to the SST (more broadly, moisture disequilibrium) controlling the variability in the air-sea enthalpy fluxes has been discussed in Jaimes et al. (2015) and Cione (2015). To assess the relative importance of SST and

10-m wind speed asymmetries on surface flux distribution in Michael, we perform a simple thought experiment where the SST is switched between dropsondes F (lowest SST) and C (maximum wind speed) from the 09H1 mission to determine how significantly the enthalpy fluxes are changed (Table 3). If the cool eddy did not exist at dropsonde F and the SST was raised from 25.58° to 27.77°C (the value at dropsonde C), the total enthalpy flux would increase from 114.6 to 383.6 W m^{-2} . That increase in enthalpy flux is larger than if the SST was held constant and the wind speed was doubled from 25.5 to 51.0 m s^{-1} . Likewise, at dropsonde C, lowering the SST to the 25.58°C value in the cool eddy lowers the enthalpy flux from 1066.8 to 517.1 W m^{-2} , a more significant reduction in enthalpy flux than if the wind speed at this location was halved from 49.95 to 24.97 m s^{-1} (leading to 532.9 W m^{-2}). Despite only a simple thought experiment, this result indicates how significantly the enthalpy fluxes can be modified by SST gradients from both warm and cool eddies.

b. Later stages of intensification

INFLUENCES OF THE ASYMMETRIC SECONDARY CIRCULATION ON PBL THERMODYNAMICS

By the third P-3 mission (09H2), Michael reached major hurricane strength while continuing to intensify. During this time the eyewall region was characterized by θ_e values of 364 – 366 K in all quadrants (Fig. 7c) and the SST was more spatially uniform than during previous missions, remaining between 28.2° and 28.4°C in the inner core (Fig. 8c). However, the storm was still interacting with a warm oceanic eddy to the southwest and cooler waters 75 km to the east and 100 km to the north of the storm center. This, combined with decreasing shear, led to a very symmetric distribution of quadrant-averaged upward motion (Figs. 6c, 13). Strong updrafts extended throughout the entire eyewall in the DSR quadrant, maximizing in the USL quadrant with sustained quadrant-averaged values greater than 2 m s^{-1} in the USR quadrant (Fig. 13). The latent heat flux maximizes at $\sim 450 \text{ W m}^{-2}$ and the sensible heat flux at $\sim 120 \text{ W m}^{-2}$ (Figs. 10e,f), though the actual maximum values were likely higher since not many eyewall dropsondes were

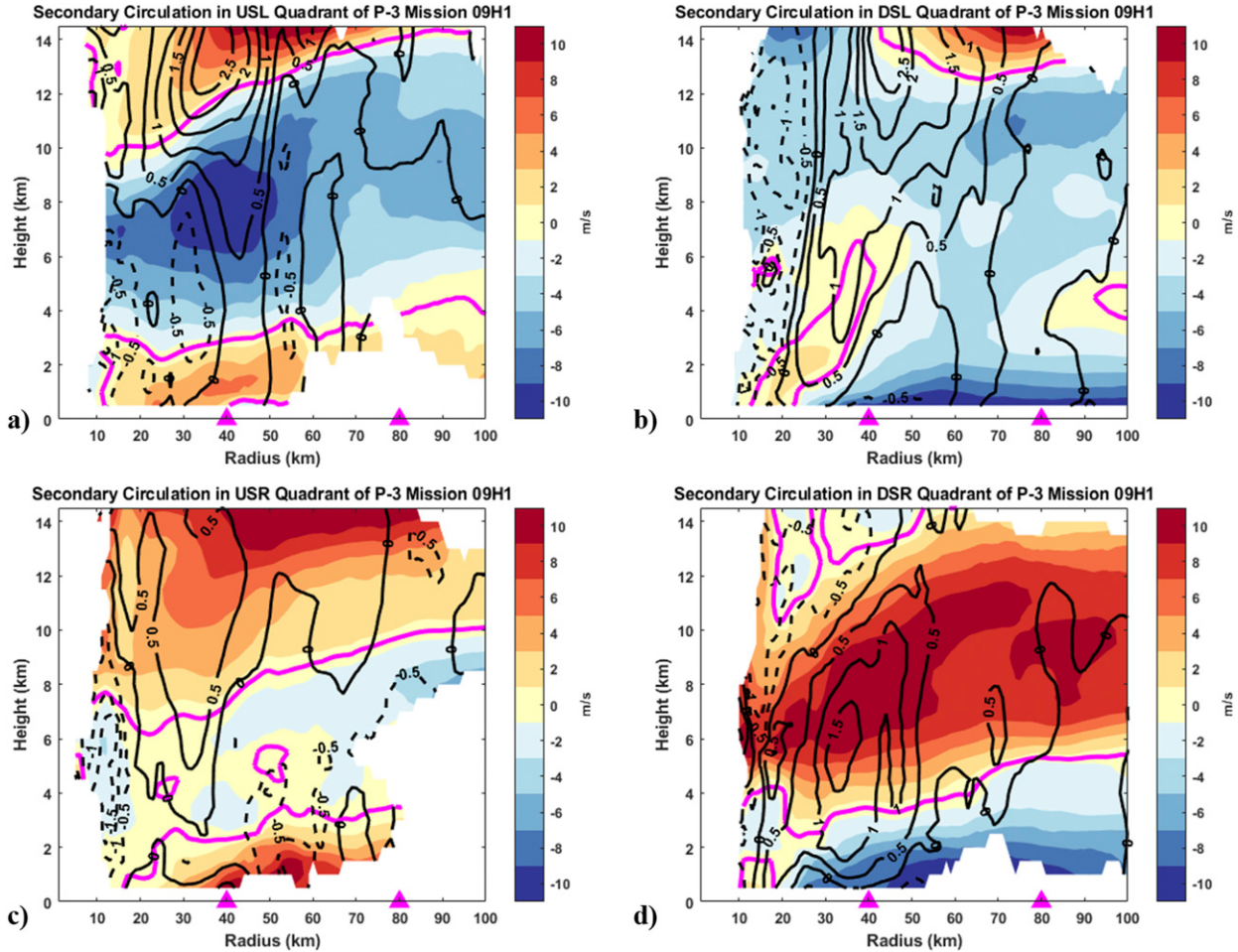


FIG. 12. Quadrant-averaged radial wind (shaded; magenta line outlines zero contour) and vertical velocity (black contoured; solid = positive and dashed = negative) in the (a) upshear-left, (b) downshear-left, (c) upshear-right, and (d) downshear-right quadrants during the 09H1 P-3 mission. The contour intervals are 1 m s^{-1} for radial wind and 0.5 m s^{-1} for vertical velocity. Pink triangles on the abscissa represent the RMW and $2 \times \text{RMW}$ at 2 km altitude. Each panel requires 40% data coverage.

released (i.e., an under sampling of the region with highest 10 m wind speeds; Fig. 9e).

While the boundary layer θ_e near the eyewall remained mostly symmetric during the 09H2 and 10H1 missions, an asymmetry was observed outside $r^* = 2$. Within 150-km radius of the DSR quadrant, the lowest observed 10 m θ_e value during either mission was 362 K (Figs. 7c,d), a value typically associated with the low-level eye and eyewall in other hurricane case studies (e.g., Zhang et al. 2017; Wadler et al. 2018b). Conversely, in the USL quadrant the lowest observed 10 m θ_e value within 150 km radius was 356 K. This is an interesting asymmetry because it is not present during the previous missions and is not reflective of SST asymmetries (Figs. 8c,d) or enthalpy flux asymmetries (Figs. 10e–h) during these sampling periods. Instead, it is related to the pronounced wavenumber-1 asymmetry in the radial wind speed between the upshear and downshear quadrants (Figs. 13 and 14).

The extent of asymmetry in the boundary layer and midlevel radial wind during the 09H2 and 10H1 missions (Figs. 13 and

14) is very similar to the composite structure for TCs experiencing shear greater than 7 m s^{-1} documented by Reasor et al. (2013; cf. their Fig. 13) and can arise because the environmental flow is different, at some levels, from the TC steering flow (Willoughby et al. 1984; Riemer and Montgomery 2011). Of particular importance is outflow originating above 4 km altitude that extended from the eyewall region to large ($>100 \text{ km}$) radii in the downshear quadrants (Figs. 13b,d and 14b,d). While the P-3 flew below the midlevel outflow layer, it was sampled by high-altitude dropsondes X, Y, Z, and T released during the 100 km radius circumnavigation period of the 09N2 mission (Fig. 15; similar time as 09H2 mission). The mean profile of radial wind from these dropsondes shows outflow in the 4–11 km layer, which is maximized at $\sim 8 \text{ m s}^{-1}$ near 6–8 km altitude (Fig. 16). This is very similar to what was observed near 100 km radius in the quadrant-averaged radar measurements in the downshear quadrants during the 09H2 mission (Figs. 13b,d), signifying that the two instruments were sampling the same quadrant-scale characteristics. In this 4–11 km layer,

TABLE 3. A list of 10 m wind speed (U_{10}), sea surface temperature (SST), latent heat flux (LHF), sensible heat flux (SHF), and total enthalpy flux (TEF) for Dropsondes C and F from the 09H1 mission. The first column shows the original observation derived values, the second column shows values for when the SST between the dropsondes is switched, and the third column shows values for when the wind speed is either halved (dropsonde C) or doubled (dropsonde F).

	Original values	Changing SST	Changing wind speed
Dropsonde C	U_{10} : 49.95 m s ⁻¹ SST: 27.77°C LHF: 817.8 W m ⁻² SHF: 248.8 W m ⁻² TEF: 1066.8 W m ⁻²	U_{10} : 49.95 m s ⁻¹ SST: 25.58°C LHF: 392.1 W m ⁻² SHF: 125.0 W m ⁻² TEF: 517.1 W m ⁻²	U_{10} : 49.95 m s ⁻¹ /2 = 24.97 m s ⁻¹ SST: 27.77°C LHF: 408.6 W m ⁻² SHF: 124.4 W m ⁻² TEF: 532.9 W m ⁻²
Dropsonde F	U_{10} : 25.5 m s ⁻¹ SST: 25.58°C LHF: 168.3 W m ⁻² SHF: -53.7 W m ⁻² TEF: 114.6 W m ⁻²	U_{10} : 25.5 m s ⁻¹ SST: 27.77°C LHF: 374.1 W m ⁻² SHF: 9.5 W m ⁻² TEF: 383.6 W m ⁻²	U_{10} : 25.5 m s ⁻¹ × 2 = 51.0 m s ⁻¹ SST: 25.58°C LHF: 336.5 W m ⁻² SHF: -107.4 W m ⁻² TEF: 229.1 W m ⁻²

the downshear dropsondes have mean θ_e values that are 3–5 K higher than the mean from upshear dropsondes U, V, and W. Expanding on what was presented in Barnes (2008) using dropsondes just outside the eyewall, we hypothesize that the

strong midlevel outflow throughout the downshear quadrants transported high-entropy air from the eyewall region outward. Outside the inner core, this thermodynamically favorable air led to positive θ_e gradients, creating a region of

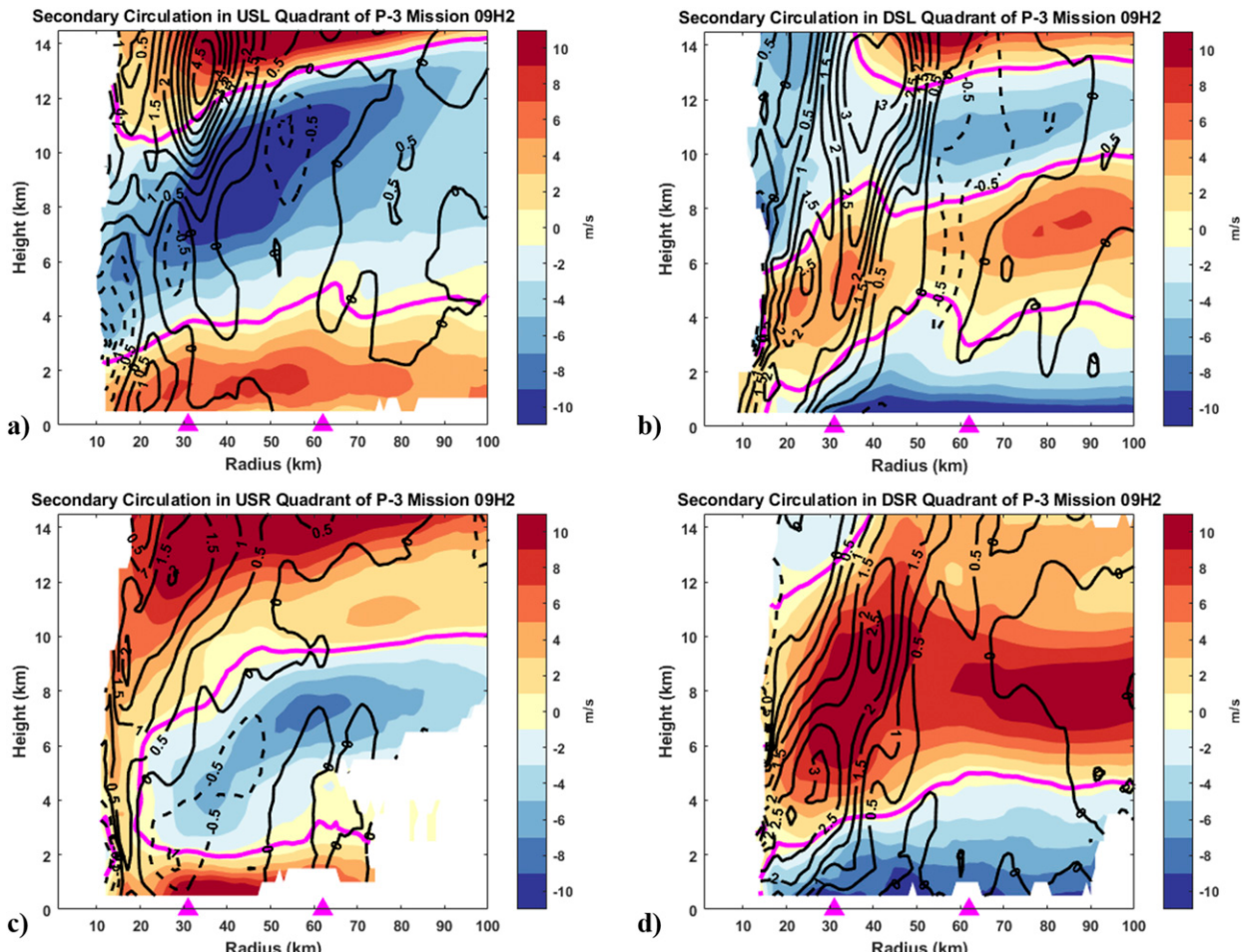


FIG. 13. As in Fig. 12, but for the 09H2 P-3 mission.

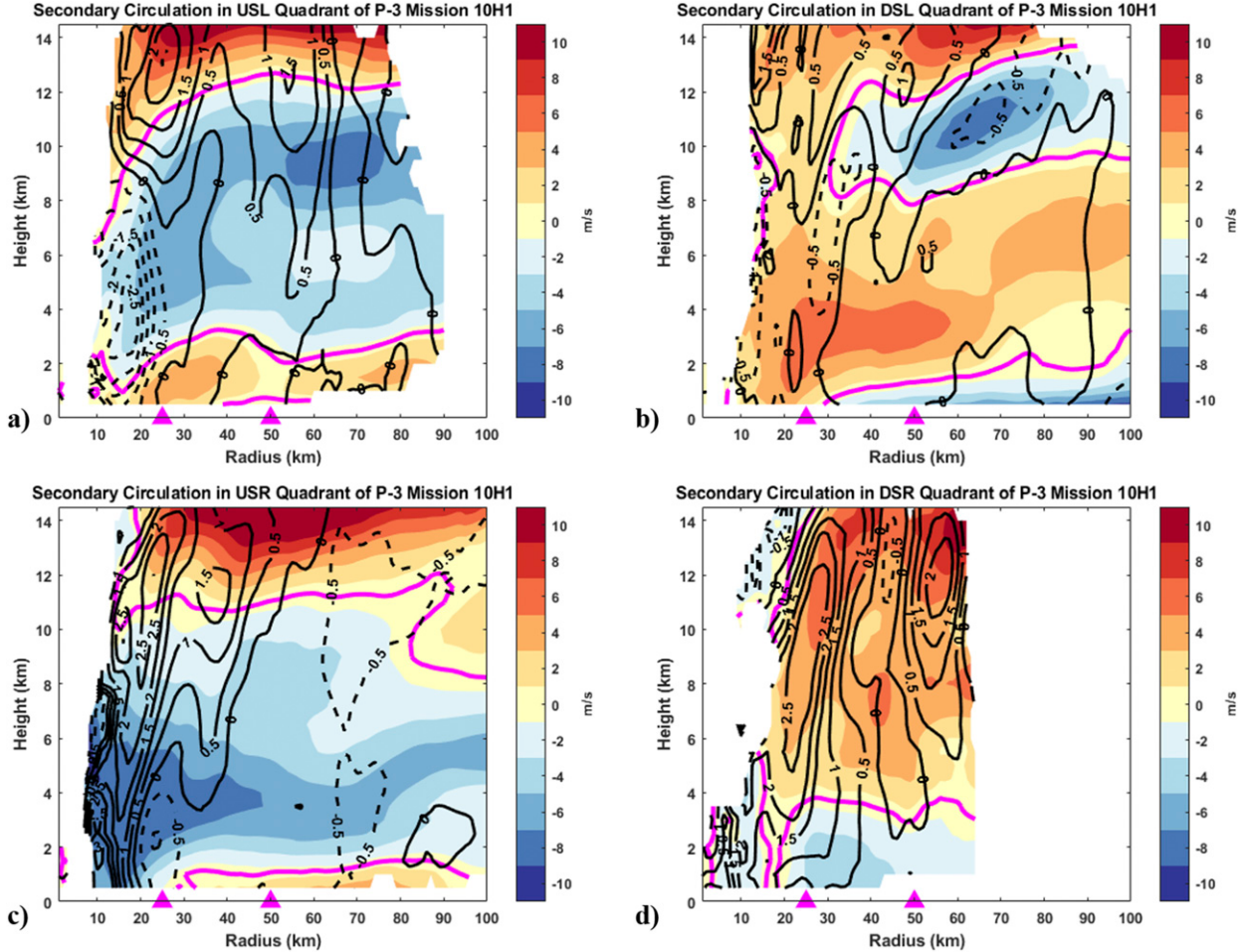


FIG. 14. As in Fig. 12, but for the 10H1 P-3 mission.

potential stability, which shielded the inflow layer against typically lower- θ_e midtropospheric air. Thus, the air associated with the outflow can be thought of as an insulator (i.e., a cap), which also allows for rapid energy increases throughout this region due to relatively large air-sea enthalpy fluxes (Hawkins and Imbembo 1976; Rotunno and Emanuel 1987; Barnes and Powell 1995; Wang et al. 2001; Wroe and Barnes 2003). The thermodynamically favorable midlevel air can also be transported back to the boundary layer by downdrafts or through entrainment across the top of the boundary layer (Anthes and Chang 1978; Kepert et al. 2016).

Radial cross sections through radar swaths at the splash locations of P-3 dropsondes released outside of the inner core (radially outward of $r^* = 2$) and outside of rainbands support the presence of midlevel outflow at locations with relatively high 10 m θ_e values in the downshear quadrants. Consistent with their respective radar-derived quadrant averages and the G-IV dropsonde means, cross sections at the dropsonde splash locations G in 09H2 and F in 10H1 reveal outflow above 4 km with inflow below (Fig. 17). The cross sections also show broad and weak descent ($<1 \text{ m s}^{-1}$)

near the dropsonde splash.² The downdrafts at the dropsonde splash location, though weak, extend between the midtroposphere (i.e., outflow layer) and the boundary layer, an indication that they can transport some of this thermodynamically favorable air back to the boundary layer. Cross sections through the splash locations of dropsondes F during 09H2 and H and X during 10H1, all locations outside of the inner-core downshear and outside of rainbands that have 10 m θ_e exceeding 360 K, have very similar characteristics (not shown).

While the midlevel outflow is not directly sampled by the P-3, profiles from dropsondes released downshear and outside the inner core show further evidence that some of the higher- θ_e air associated with the outflow from the eyewall was being transported downward. These dropsondes have a layer

² It is worth noting that there is added uncertainty in vertical velocity values from the airborne Doppler radar when the velocities are weak (Reasor et al. 2009). While there is uncertainty in the exact values, there is still confidence that the vertical velocities at these locations are weak, signifying the favorable air is in mostly horizontal motion and insulating the boundary layer.

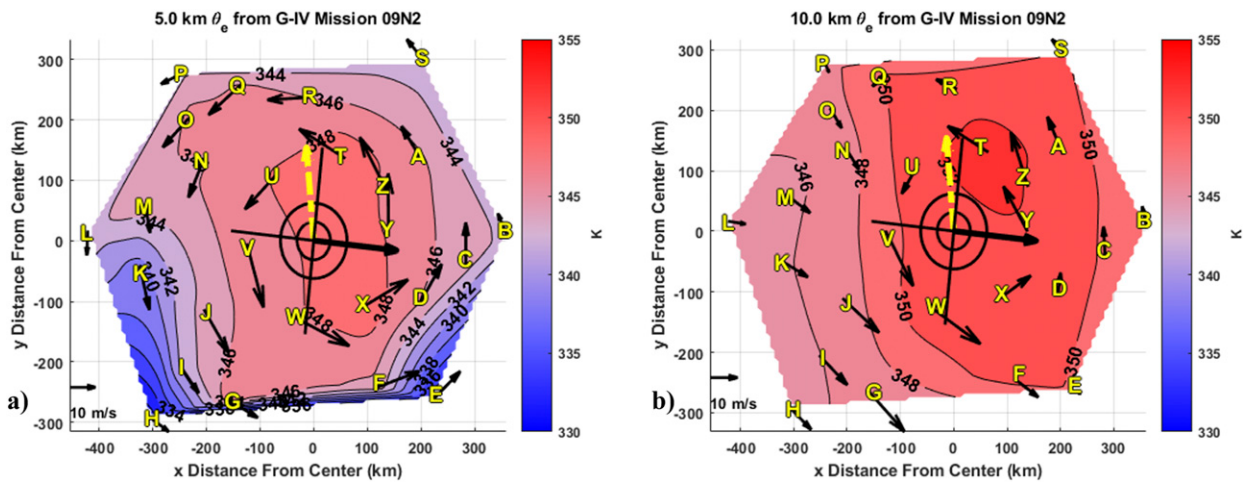


FIG. 15. As in Fig. 2, but for equivalent potential temperature (θ_e) at (a) 5.0 and (b) 10.0 km from dropsondes released during G-IV mission 09N2.

between 100 and 500 m thick (within the lowest 2500 m), which has an increase in θ_e with height (Fig. 18a), coincident with decreasing inflow strength with height (Fig. 18b). While yielding a narrower perspective than the G-IV dropsondes and radar cross sections, these dropsonde profiles are like those identified by Barnes (2008), who concluded that the only reasonable explanation for a positive lapse rate in θ_e above the surface layer is differential advection of the radial wind, by which the midlevel higher- θ_e air is transported outward from the eyewall or rainbands.

Another interesting characteristic in the 10 m θ_e during the 09H2 and 10H1 missions is the relatively high values at large radii in the USR quadrant (Figs. 7c,d). Similar to the midlevels, the layer between 0.5 and 2 km was characterized by shear-relative asymmetries in the secondary circulation between the downshear and upshear quadrants. In this layer, both the quadrant-averaged radar cross sections (Figs. 13 and 14) and

composite dropsonde observations from upshear dropsondes U, V, and W, released during the 100-km circumnavigation period of the 09N2 mission (Fig. 16) show that the upshear (downshear) quadrants are characterized by outflow (inflow). The G-IV dropsondes also show that the low-level outflow layer between 0.5 and 2 km altitude upshear is associated with 3–5 K higher θ_e values than that in the downshear quadrants (Fig. 16). We hypothesize that the low-level outflow throughout the upshear quadrants transports high-entropy air away from the eyewall region outward where, consistent with processes occurring in the midlevels downshear, leads to weaker vertical θ_e gradients (between 0.5 and 1 km in Fig. 16) and an insulation of the shallow (<500 m) inflow layer from drier midlevel air. The favorable air in this region also serves a secondary purpose by complementing the air-sea enthalpy fluxes for recovery of θ_e from low-entropy downdrafts that typically occur upwind in the left-of-shear quadrants.

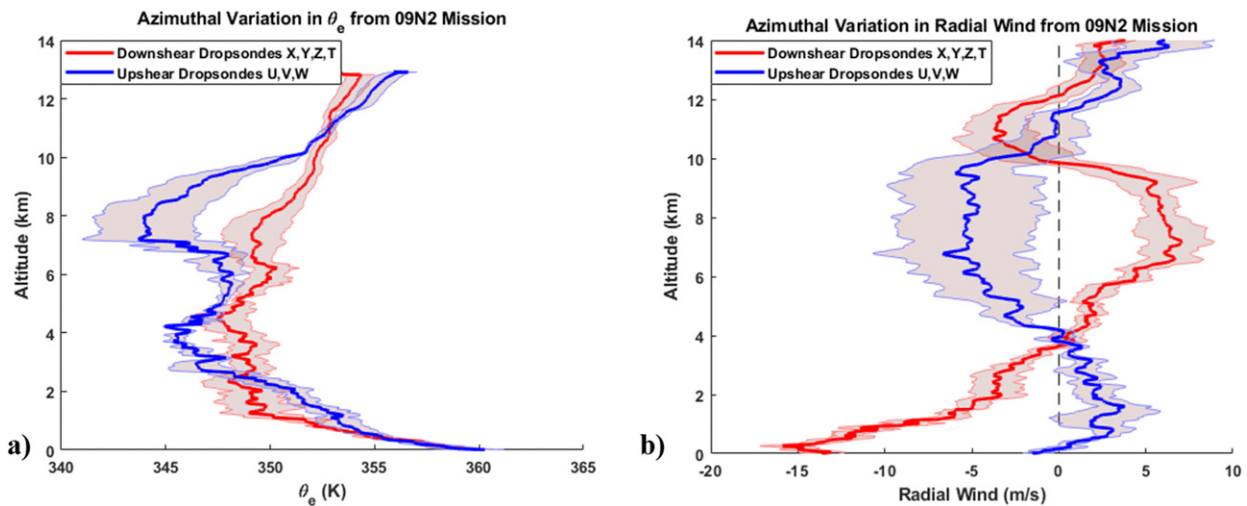


FIG. 16. The average (line) and standard error (shaded) of (a) θ_e and (b) radial wind between downshear dropsondes X, Y, Z, and T and upshear dropsondes U, V, and W from the 09N2 G-IV mission.

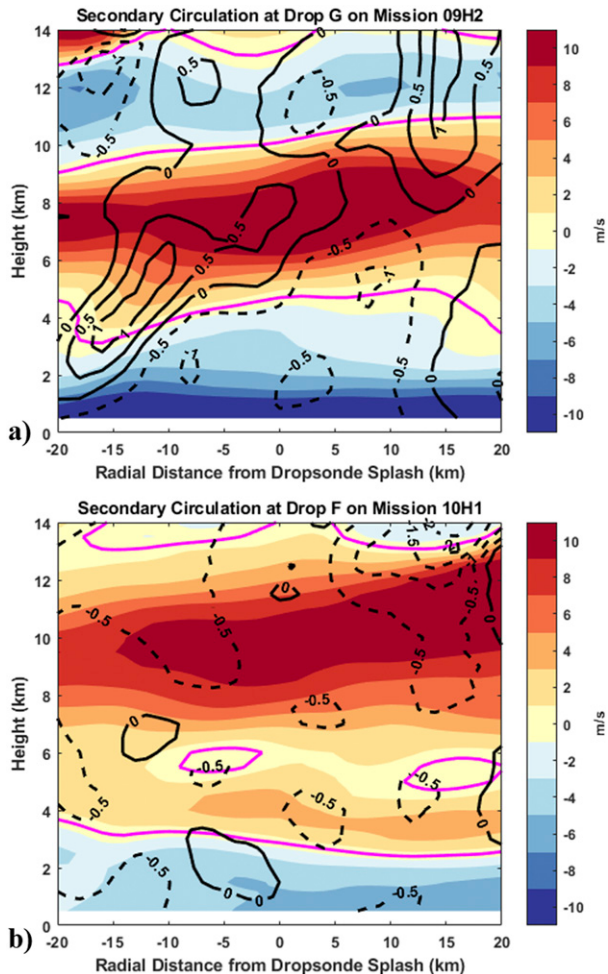


FIG. 17. Radial cross section through the radar swath (negative values on abscissa being closer to TC center) of radial velocity (shaded with thick magenta line showing zero contour) and vertical velocity (contoured with solid lines = positive; dashed lines = negative) through the splash location of (a) dropsonde G located in the downshear-left quadrant during the 09H2 P-3 mission and (b) dropsonde F located in the downshear-right quadrant during the 10H1 P-3 mission. The contour interval is 5 m s^{-1} for radial velocity and 0.5 m s^{-1} for vertical velocity.

The processes that occurred at the P-3 dropsonde splash locations support this hypothesis. Radial cross sections through the radar swaths at the splash locations of dropsondes M in 09H2 and P in 10H1 show that the low-level outflow was below 1.5–2.0 km, with inflow above, coincident with broad areas of weak subsidence ($<1.0 \text{ m s}^{-1}$; Fig. 19). The radar cross sections through the splash locations of dropsondes J, S during the 09H2 mission and P during the 10H1 mission, all upshear locations with relatively high $10\text{m } \theta_e$ values, had similar characteristics (not shown).

4. Discussion and conclusions

This study synthesizes kinematic, thermodynamic, and oceanic observations to examine the rapid intensification of

Hurricane Michael (2018) through the complex multiscale interaction between environmental influences, distribution of convection and precipitation, boundary layer thermodynamics, air-sea interaction, and storm structure. Dropsondes released from the high altitude G-IV aircraft during the early stage of RI in the southern Gulf of Mexico show that dry air from the northwest was not significantly entrained into the storm circulation within 200 km radius from the storm center.

During all missions, the airborne pseudo-dual-Doppler radar indicates that the altitude of peak upward motion was lowest in the downshear quadrants (convection likely initiating there) and highest in the USL quadrant. Importantly, the convection was able to form downshear during the first two missions, even though that was in the region of relatively cool SSTs ($\sim 25.5^\circ\text{C}$) due to a cool oceanic eddy. The presence of the cool waters was significant, as a simple thought experiment showed that the reduced SST associated with the cool eddy led to a greater reduction in the enthalpy fluxes than if the wind speed were halved. With these observations, we hypothesize that for RI to occur, it is most important to have warm waters in the left-of-shear quadrants to directly aid the sustainment of convection into the upshear quadrants (assuming the midlevel humidity and stability profiles are also favorable) and for quick boundary layer recovery from any low- θ_e downdraft air.

With enhanced enthalpy fluxes for quick boundary layer recovery, the DSR quadrant is characterized by high θ_e values, favoring convective development in the region of tilt-induced mechanical ascent. This is consistent with a recent dropsonde composite study of weak TCs by Nguyen et al. (2019), which found that intensifying TCs have higher enthalpy fluxes in the upshear quadrants than nonintensifying TCs. While there are no direct observations, we speculate that the opposite orientation of the oceanic thermal gradients relative to the shear vector (i.e., coolest waters left of shear) would not be as favorable for intensification. Between the 08H1 and 09H1 missions, when the oceanic cool eddy was on the northern (left of shear) side of the vortex, Michael maintained near-constant intensity (Fig. 1a). While, in this scenario, enhanced enthalpy fluxes in the right-of-shear quadrants could support boundary layer recovery, the time low- θ_e parcels have over warm waters to recover may be limited before they reach the typical convective initiation regions. Additionally, suppressed enthalpy fluxes in the left-of-shear quadrants could limit the propagation of convection and precipitation into the upshear quadrants. Note a similar enthalpy flux distribution was found to be unfavorable for TC genesis in Rappin and Nolan (2012). Further testing the role of SST gradients in modulating the near-surface θ_e and convective distribution is needed through numerical simulations and other case studies.

As RI continued during the two P-3 missions before landfall, Michael had an asymmetric secondary circulation that was qualitatively similar to the composites shown by Reasor et al. (2013), and likely resulted from differences between the environmental flow and TC steering flow (e.g., Willoughby et al. 1984; Riemer and Montgomery 2011). High-altitude dropsondes from a 100 km radius circumnavigation during the G-IV mission show that the downshear midlevel outflow region has a mean θ_e that is 3–5 K larger than that at the same altitude of the

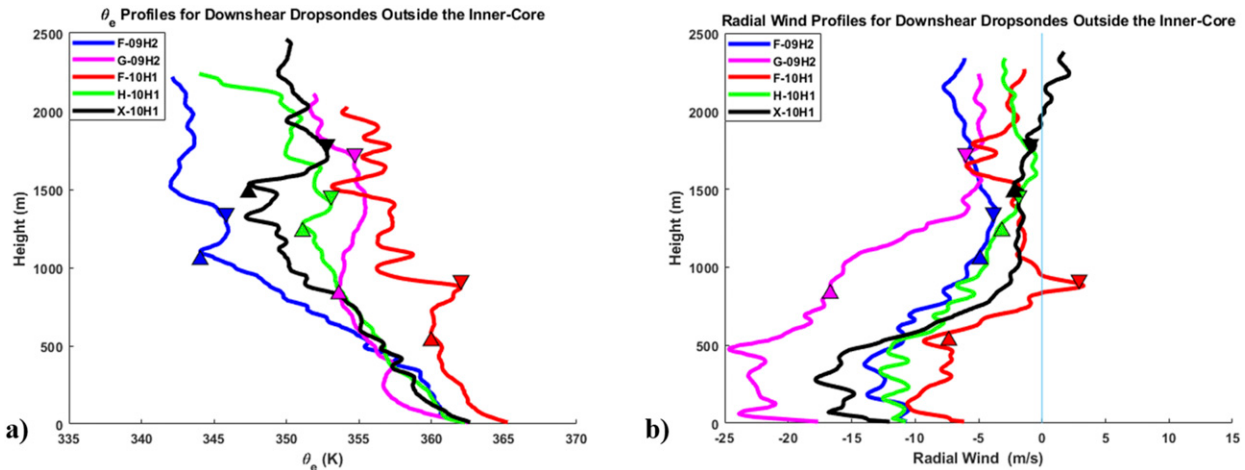


FIG. 18. Quasi-vertical profiles of (a) θ_e and (b) radial wind for downshear dropsondes with favorable 10 m θ_e values and locations where radar cross sections through the dropsonde splash locations reveal midlevel outflow. Up and down triangles indicate bounds for regions of increasing θ_e with height, coincident with decreasing inflow strength with height.

upshear quadrants. Coincidentally, dropsondes released from the P-3 downshear and outside of the inner core reveal that this region has a maximum in 10 m θ_e . Radial cross sections through radar swaths at the downshear dropsonde splash locations reveal broad areas of weak nonconvective subsidence. Combining these measurements, we argue that the strong ($>10 \text{ m s}^{-1}$) midlevel outflow from the eyewall region containing high- θ_e air can insulate the boundary layer as the air is transported outward throughout the downshear quadrants through lowering vertical θ_e gradients and creating convective stability. This relatively favorable air can also be brought back into the inflow layer through the weak subsidence and entrainment across the top of the boundary layer. The transport of high- θ_e air to large radii by midlevel outflow is supported by a recent idealized modeling study by Li and Dai (2020), which also found that the midlevel maximum in θ_e led to potential stability in the outer core of the downshear quadrants.

The transport and entrainment of this high- θ_e air into the boundary layer is supported by the individual dropsonde profiles from the P-3 at different downshear locations, each showing a layer with increasing θ_e with height, coincident with decreasing inflow (or outflow). This pattern extrapolates what was noticed in Barnes and Powell (1995) and Barnes (2008) for individual dropsondes to the shear-relative structure of a mature TC, and suggests that the processes identified by Barnes (2008) can be extrapolated beyond just outside the eyewall and rainband regions in a strong storm with a well-developed asymmetric secondary circulation. To transport the midlevel air a significant distance from the inner core, we speculate this process is limited to strong hurricanes, which can have large radial wind magnitudes. With the G-IV circumnavigations at 100 km farther radius during the first two missions than during 09N2, it is unknown if the outflow insulates the boundary layer to large radii earlier in Michael's life cycle.

On the upshear side of the storm, high- θ_e air was also noticed in the boundary layer and attributed to outflow from the eyewall, but between 0.5 and 2 km altitude. As discussed by

Balachandran et al. (2019), even though this low-level outflow upshear (again characteristic of hurricanes in shear) signifies a net mass flux away from the eyewall and does not directly influence the entropy of the air that enters the eyewall, it can insulate the shallow (<500 m) inflow layer from generally low- θ_e midtropospheric air. Additionally, because the azimuthal location is downwind of where convective downdrafts typically transport low-entropy air to the boundary layer (i.e., Riemer et al. 2010), the low level-outflow in the DSR quadrant can complement the boundary layer recovery process due to the air-sea enthalpy fluxes, which tends to occur in this region (i.e., Zhang et al. 2013).

The results from this study build upon the Riemer et al. (2010) theory that describes how shear influences TC intensity change by understanding how the secondary circulation modifies the midlevel temperature and humidity. In theory, convective downdrafts transport thermodynamically unfavorable midtropospheric air into the boundary layer, which can be entrained into the eyewall and subsequently limit convection and weaken the vortex. In a sheared vortex, the midlevel outflow from the eyewall in the downshear quadrants may limit the amount of typically low- θ_e midtropospheric air that is present, especially when the storm is over favorable oceanic conditions and resilient to entrainment of environmental dry air. While this process positively influences the inflow layer θ_e , which is favorable for TC intensification, what remains unclear is how significantly the detrainment of high- θ_e air from the eyewall region negatively influences eyewall buoyancy and latent heat release. That is a topic of a future modeling study.

While we showed a pathway for weak downdrafts to transport high-entropy air to the boundary layer, it should be noted that without dropsonde observations it is unclear how the thermodynamically favorable midlevel air is modified inside convective downdrafts and rainband regions, where the flow varies on the convective-scale (e.g., Powell 1990; Didlake and Houze 2009). Additionally, it is unclear how sensitive these processes are to the shape of the radial variation in the wind

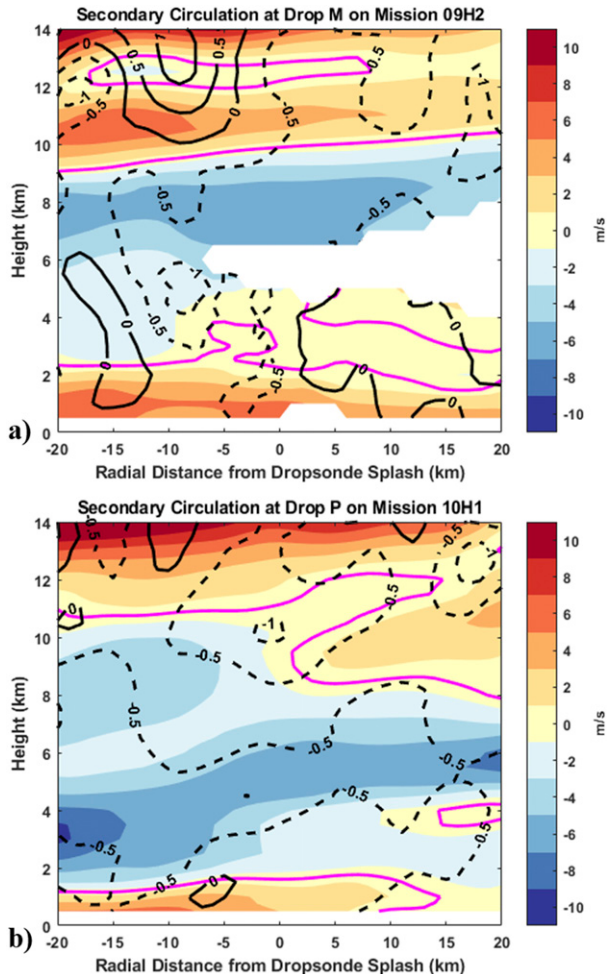


FIG. 19. As in Fig. 17, but for (a) dropsonde M located in the upshear-right quadrant during 09H2 P-3 mission and (b) dropsonde P located in the upshear-right quadrant during 10H1 P-3 mission.

field (e.g., inertial stability) and environmental conditions such as shear magnitude and direction, which can have a significant impact on storm structure and intensity (e.g., Reasor and Eastin 2012; Ge et al. 2013; Zhang and Tao 2013; Tao and Zhang 2014; Finocchio et al. 2016; Miyamoto and Nolan 2018; Rios-Berrios et al. 2018). More case studies with targeted observations are needed to explore these processes.

Acknowledgments. The measurements presented in this manuscript would not have been obtained without the staff of NOAA's Aircraft Operations Center (AOC). The authors greatly appreciate the comments and suggestions from Dr. Jonathan Zawislak of AOML/HRD and four anonymous reviewers. This work was completed while Joshua Wadler was gratefully supported by a National Science Foundation Graduate Research Fellowship under Grant DGE-1451511. Jun Zhang is supported by NSF Grant AGS-1822128, ONR Grant N00014-20-1-2071, and NOAA Grant NA19OAR4590239. Benjamin Jaimes and Lynn Shay are gratefully supported by the National Science Foundation under Grant AGS 19-41498.

REFERENCES

- Aberson, S. D., M. T. Montgomery, M. M. Bell, and M. L. Black, 2006: Hurricane Isabel (2003): New insights into the physics of intense storms. Part II: Extreme localized wind. *Bull. Amer. Meteor. Soc.*, **87**, 1349–1354, <https://doi.org/10.1175/BAMS-87-10-1349>.
- Alland, J. J., B. H. Tang, and K. L. Corbosiero, 2017: Effects of midlevel dry air on development of the axisymmetric tropical cyclone secondary circulation. *J. Atmos. Sci.*, **74**, 1455–1470, <https://doi.org/10.1175/JAS-D-16-0271.1>.
- Alvey, G. R., III, J. Zawislak, and E. Zipser, 2015: Precipitation properties observed during tropical cyclone intensity change. *Mon. Wea. Rev.*, **143**, 4476–4492, <https://doi.org/10.1175/MWR-D-15-0065.1>.
- , E. Zipser, and J. Zawislak, 2020: How does Hurricane Edouard (2014) evolve toward symmetry before rapid intensification? A high-resolution ensemble study. *J. Atmos. Sci.*, **77**, 1329–1351, <https://doi.org/10.1175/JAS-D-18-0355.1>.
- Anthes, R. A., and S. Chang, 1978: Response of the hurricane boundary layer to changes of sea surface temperature in a numerical model. *J. Atmos. Sci.*, **35**, 1240–1255, [https://doi.org/10.1175/1520-0469\(1978\)035<1240:ROTHBL>2.0.CO;2](https://doi.org/10.1175/1520-0469(1978)035<1240:ROTHBL>2.0.CO;2).
- Balaguru, K., G. R. Foltz, L. R. Leung, J. Kaplan, W. Xu, N. Reul, and B. Chapron, 2020: Pronounced impact of salinity on rapidly intensifying tropical cyclones. *Bull. Amer. Meteor. Soc.*, **101**, E1497–E1511, <https://doi.org/10.1175/BAMS-D-19-0303.1>.
- Barnes, G. M., 2008: Atypical thermodynamic profiles in hurricanes. *Mon. Wea. Rev.*, **136**, 631–643, <https://doi.org/10.1175/2007MWR2033.1>.
- , and M. D. Powell, 1995: Evolution of the inflow boundary layer of Hurricane Gilbert (1988). *Mon. Wea. Rev.*, **123**, 2348–2368, [https://doi.org/10.1175/1520-0493\(1995\)123<2348:EOTIBL>2.0.CO;2](https://doi.org/10.1175/1520-0493(1995)123<2348:EOTIBL>2.0.CO;2).
- , and P. Fuentes, 2010: Eye excess energy and the rapid intensification of Hurricane Lili (2002). *Mon. Wea. Rev.*, **138**, 1446–1458, <https://doi.org/10.1175/2009MWR3145.1>.
- , and K. P. Dolling, 2013: The inflow to Tropical Cyclone Humberto (2001) as viewed with azimuth–height surfaces over three days. *Mon. Wea. Rev.*, **141**, 1324–1336, <https://doi.org/10.1175/MWR-D-11-00348.1>.
- , E. J. Zipser, D. Jorgensen, and F. D. Marks, 1983: Mesoscale and convective structure of a hurricane rainband. *J. Atmos. Sci.*, **40**, 2125–2137, [https://doi.org/10.1175/1520-0469\(1983\)040<2125:MACSOA>2.0.CO;2](https://doi.org/10.1175/1520-0469(1983)040<2125:MACSOA>2.0.CO;2).
- Bell, M. M., and M. T. Montgomery, 2008: Observed structure, evolution and potential intensity of category 5 Hurricane Isabel (2003) from 12 to 14 September. *Mon. Wea. Rev.*, **136**, 2023–2046, <https://doi.org/10.1175/2007MWR1858.1>.
- Beven, J. L., II, R. Berg, and A. Hagen, 2019: Tropical cyclone report: Hurricane Michael (7–11 October 2018). NHC Tech. Rep. AL142018, 86 pp., https://www.nhc.noaa.gov/data/tcr/AL142018_Michael.pdf.
- Bhalachandran, S., R. Nadimpalli, K. K. Osuri, F. D. Marks Jr., S. Gopalakrishnan, S. Subramanian, U. C. Mohanty, and D. Niyogi, 2019: On the processes influencing rapid intensity changes of tropical cyclones over the Bay of Bengal. *Sci. Rep.*, **9**, 3382, <https://doi.org/10.1038/s41598-019-40332-z>.
- Bolton, D., 1980: The computation of equivalent potential temperature. *Mon. Wea. Rev.*, **108**, 1046–1053, [https://doi.org/10.1175/1520-0493\(1980\)108<1046:TCOEPT>2.0.CO;2](https://doi.org/10.1175/1520-0493(1980)108<1046:TCOEPT>2.0.CO;2).
- Boyd, J., 1987: Improved depth and temperature conversion equations for Sippican AXBTs. *J. Atmos. Oceanic Technol.*,

- 4, 545–551, [https://doi.org/10.1175/1520-0426\(1987\)004<0545:IDATCE>2.0.CO;2](https://doi.org/10.1175/1520-0426(1987)004<0545:IDATCE>2.0.CO;2).
- Cecil, D. J., and T. Chronis, 2018: Polarization-corrected temperatures for 10-, 19-, 37-, and 89-GHz passive microwave frequencies. *J. Appl. Meteor. Climatol.*, **57**, 2249–2265, <https://doi.org/10.1175/JAMC-D-18-0022.1>.
- Chen, H., and S. G. Gopalakrishnan, 2015: A study on the asymmetric rapid intensification of Hurricane Earl (2010) using the HWRF system. *J. Atmos. Sci.*, **72**, 531–550, <https://doi.org/10.1175/JAS-D-14-0097.1>.
- Chen, S. S., W. Zhao, M. A. Donelan, and H. L. Tolman, 2013: Directional wind-wave coupling in fully coupled atmosphere-wave-ocean models: Results from CBLAST-Hurricane. *J. Atmos. Sci.*, **70**, 3198–3215, <https://doi.org/10.1175/JAS-D-12-0157.1>.
- Cione, J. J., 2015: The relative roles of the ocean and atmosphere as revealed by buoy air-sea observations in hurricanes. *Mon. Wea. Rev.*, **143**, 904–913, <https://doi.org/10.1175/MWR-D-13-00380.1>.
- , P. G. Black, and S. H. Houston, 2000: Surface observations in the hurricane environment. *Mon. Wea. Rev.*, **128**, 1550–1561, [https://doi.org/10.1175/1520-0493\(2000\)128<1550:SOITHE>2.0.CO;2](https://doi.org/10.1175/1520-0493(2000)128<1550:SOITHE>2.0.CO;2).
- , E. A. Kalina, J. A. Zhang, and E. W. Uhlhorn, 2013: Observations of air-sea interaction and intensity change in hurricanes. *Mon. Wea. Rev.*, **141**, 2368–2382, <https://doi.org/10.1175/MWR-D-12-00070.1>.
- Cram, T. A., J. Persing, M. T. Montgomery, and S. A. Braun, 2007: A Lagrangian trajectory view on transport and mixing processes between the eye, eyewall, and environment using a high-resolution simulation of Hurricane Bonnie (1998). *J. Atmos. Sci.*, **64**, 1835–1856, <https://doi.org/10.1175/JAS3921.1>.
- Dai, Y., S. J. Majumdar, and D. S. Nolan, 2019: The outflow-rainband relationship induced by environmental flow around tropical cyclones. *J. Atmos. Sci.*, **76**, 1845–1863, <https://doi.org/10.1175/JAS-D-18-0208.1>.
- DeHart, J. C., R. A. Houze, and R. F. Rogers, 2014: Quadrant distribution of tropical cyclone inner-core kinematics in relation to environmental shear. *J. Atmos. Sci.*, **71**, 2713–2732, <https://doi.org/10.1175/JAS-D-13-0298.1>.
- DeMaria, M., and J. Kaplan, 1999: An updated Statistical Hurricane Intensity Prediction Scheme (SHIPS) for the Atlantic and eastern North Pacific basins. *Wea. Forecasting*, **14**, 326–337, [https://doi.org/10.1175/1520-0434\(1999\)014<0326:AUSHIP>2.0.CO;2](https://doi.org/10.1175/1520-0434(1999)014<0326:AUSHIP>2.0.CO;2).
- Didlake, A. C., and R. A. Houze, 2009: Convective-scale down-drafts in the principal rainband of Hurricane Katrina (2005). *Mon. Wea. Rev.*, **137**, 3269–3293, <https://doi.org/10.1175/2009MWR2827.1>.
- , and —, 2013: Dynamics of the stratiform sector of a tropical cyclone rainband. *J. Atmos. Sci.*, **70**, 1891–1911, <https://doi.org/10.1175/JAS-D-12-0245.1>.
- , P. D. Reasor, R. F. Rogers, and W. Lee, 2018: Dynamics of the transition from spiral rainbands to a secondary eyewall in Hurricane Earl (2010). *J. Atmos. Sci.*, **75**, 2909–2929, <https://doi.org/10.1175/JAS-D-17-0348.1>.
- Dolling, K. P., and G. M. Barnes, 2012: The creation of a high equivalent potential temperature reservoir in Tropical Storm Humberto (2001) and its possible role in storm deepening. *Mon. Wea. Rev.*, **140**, 492–505, <https://doi.org/10.1175/MWR-D-11-00068.1>.
- , and —, 2014: The evolution of Hurricane Humberto (2001). *J. Atmos. Sci.*, **71**, 1276–1291, <https://doi.org/10.1175/JAS-D-13-0164.1>.
- Eastin, M. D., W. M. Gray, and P. G. Black, 2005a: Buoyancy of convective vertical motions in the inner core of intense hurricanes. Part I: General statistics. *Mon. Wea. Rev.*, **133**, 188–208, <https://doi.org/10.1175/MWR-2848.1>.
- , —, and —, 2005b: Buoyancy of convective vertical motions in the inner core of intense hurricanes. Part II: Case studies. *Mon. Wea. Rev.*, **133**, 209–227, <https://doi.org/10.1175/MWR-2849.1>.
- , T. L. Gardner, M. C. Link, and K. C. Smith, 2012: Surface cold pools in the outer rainbands of Tropical Storm Hanna (2008) near landfall. *Mon. Wea. Rev.*, **140**, 471–491, <https://doi.org/10.1175/MWR-D-11-00099.1>.
- Emanuel, K. A., 1986: An air-sea interaction theory for tropical cyclones. Part I: Steady-state maintenance. *J. Atmos. Sci.*, **43**, 585–605, [https://doi.org/10.1175/1520-0469\(1986\)043<0585:AASITF>2.0.CO;2](https://doi.org/10.1175/1520-0469(1986)043<0585:AASITF>2.0.CO;2).
- Finocchio, P. M., S. J. Majumdar, D. S. Nolan, and M. Iskandarani, 2016: Idealized tropical cyclone responses to the height and depth of environmental vertical wind shear. *Mon. Wea. Rev.*, **144**, 2155–2175, <https://doi.org/10.1175/MWR-D-15-0320.1>.
- Fischer, M. S., R. F. Rogers, and P. D. Reasor, 2020: The rapid intensification and eyewall replacement cycles of Hurricane Irma (2017). *Mon. Wea. Rev.*, **148**, 981–1004, <https://doi.org/10.1175/MWR-D-19-0185.1>.
- Gamache, J. F., 1997: Evaluation of a fully three-dimensional variational Doppler analysis technique. *Preprints, 28th Conf. on Radar Meteorology*, Austin, TX, Amer. Meteor. Soc., 422–423.
- Ge, X., T. Li, and M. Peng, 2013: Effects of vertical shears and midlevel dry air on tropical cyclone developments. *J. Atmos. Sci.*, **70**, 3859–3875, <https://doi.org/10.1175/JAS-D-13-066.1>.
- Guimond, S. R., G. M. Heymsfield, P. D. Reasor, and A. C. Didlake Jr., 2016: The rapid intensification of Hurricane Karl (2010): New remote sensing observations of convective bursts from the Global Hawk platform. *J. Atmos. Sci.*, **73**, 3617–3639, <https://doi.org/10.1175/JAS-D-16-0026.1>.
- Hallowell, G. R., L. K. Shay, J. K. Brewster, and W. J. Teague, 2011: Evaluation and sensitivity analysis of an ocean model response to Hurricane Ivan. *Mon. Wea. Rev.*, **139**, 921–945, <https://doi.org/10.1175/2010MWR3104.1>.
- , S. Gopalakrishnan, F. Marks, and D. Willey, 2015: Idealized study of ocean impacts on tropical cyclone intensity forecasts. *Mon. Wea. Rev.*, **143**, 1142–1165, <https://doi.org/10.1175/MWR-D-14-00022.1>.
- Hamilton, P., 1992: Lower continental slope cyclonic eddies in the central Gulf of Mexico. *J. Geophys. Res.*, **97**, 2185–2200, <https://doi.org/10.1029/91JC01496>.
- Hankin, S., J. Callahan, A. Manke, K. O'Brien, and J. Li, 2006: Ferret user's guide version 6.0. NOAA/Pacific Marine Environmental Laboratory, 592 pp., https://dav.lbl.gov/archive/NERSC/Software/ferret/docs/ferret_users_guide_v600.pdf.
- Hawkins, H. F., and S. M. Imbembo, 1976: The structure of a small, intense hurricane, Inez, 1966. *Mon. Wea. Rev.*, **104**, 418–442, [https://doi.org/10.1175/1520-0493\(1976\)104<0418:TSOASI>2.0.CO;2](https://doi.org/10.1175/1520-0493(1976)104<0418:TSOASI>2.0.CO;2).
- Hazelton, A. T., R. E. Hart, and R. F. Rogers, 2017: Analyzing simulated convective bursts in two Atlantic hurricanes. Part II: Intensity change due to bursts. *Mon. Wea. Rev.*, **145**, 3095–3117, <https://doi.org/10.1175/MWR-D-16-0268.1>.
- Hlywiak, J., and D. S. Nolan, 2019: The influence of oceanic barrier layers on tropical cyclone intensity as determined through idealized, coupled numerical simulations. *J. Phys. Oceanogr.*, **49**, 1723–1745, <https://doi.org/10.1175/JPO-D-18-0267.1>.

- Hock, T. F., and J. L. Franklin, 1999: The NCAR GPS dropwindsonde. *Bull. Amer. Meteor. Soc.*, **80**, 407–420, [https://doi.org/10.1175/1520-0477\(1999\)080<0407:TNGD>2.0.CO;2](https://doi.org/10.1175/1520-0477(1999)080<0407:TNGD>2.0.CO;2).
- Hong, X., S. W. Chang, S. Raman, L. K. Shay, and R. Hodur, 2000: The interaction between Hurricane Opal (1995) and a warm core ring in the Gulf of Mexico. *Mon. Wea. Rev.*, **128**, 1347–1365, [https://doi.org/10.1175/1520-0493\(2000\)128<1347:TIBHOA>2.0.CO;2](https://doi.org/10.1175/1520-0493(2000)128<1347:TIBHOA>2.0.CO;2).
- Jacob, S. D., L. K. Shay, A. J. Mariano, and P. G. Black, 2000: The 3D mixed layer response to Hurricane Gilbert. *J. Phys. Oceanogr.*, **30**, 1407–1429, [https://doi.org/10.1175/1520-0485\(2000\)030<1407:TOTMLRT>2.0.CO;2](https://doi.org/10.1175/1520-0485(2000)030<1407:TOTMLRT>2.0.CO;2).
- Jaimes, B., and L. K. Shay, 2009: Mixed layer cooling in mesoscale oceanic eddies during Hurricanes Katrina and Rita. *Mon. Wea. Rev.*, **137**, 4188–4207, <https://doi.org/10.1175/2009MWR2849.1>.
- , —, 2010: Near-inertial wave wake of Hurricanes Katrina and Rita over mesoscale oceanic eddies. *J. Phys. Oceanogr.*, **40**, 1320–1337, <https://doi.org/10.1175/2010JPO4309.1>.
- , —, 2015: Enhanced wind-driven downwelling flow in warm oceanic eddy features during the intensification of Tropical Cyclone Isaac (2012): Observations and theory. *J. Phys. Oceanogr.*, **45**, 1667–1689, <https://doi.org/10.1175/JPO-D-14-0176.1>.
- , —, and E. W. Uhlhorn, 2015: Enthalpy and momentum fluxes during Hurricane Earl relative to underlying ocean features. *Mon. Wea. Rev.*, **143**, 111–131, <https://doi.org/10.1175/MWR-D-13-00277.1>.
- , —, and J. K. Brewster, 2016: Observed air-sea interactions in tropical cyclone Isaac over loop current mesoscale eddy features. *Dyn. Atmos. Oceans*, **76**, 306–324, <https://doi.org/10.1016/j.dynatmoe.2016.03.001>.
- Jiang, H., 2012: The relationship between tropical cyclone intensity change and the strength of inner-core convection. *Mon. Wea. Rev.*, **140**, 1164–1176, <https://doi.org/10.1175/MWR-D-11-00134.1>.
- , J. P. Zagrodnik, C. Tao, and E. J. Zipser, 2018: Classifying precipitation types in tropical cyclones using the NRL 37 GHz color product. *J. Geophys. Res. Atmos.*, **123**, 5509–5524, <https://doi.org/10.1029/2018JD028324>.
- Johnson, G. C., 1995: Revised XCTD fall-rate equation coefficients from CTD data. *J. Atmos. Oceanic Technol.*, **12**, 1367–1373, [https://doi.org/10.1175/1520-0426\(1995\)012<1367:RXFREC>2.0.CO;2](https://doi.org/10.1175/1520-0426(1995)012<1367:RXFREC>2.0.CO;2).
- Jones, S. C., 1995: The evolution of vortices in vertical shear: Initially barotropic vortices. *Quart. J. Roy. Meteor. Soc.*, **121**, 821–851, <https://doi.org/10.1002/qj.49712152406>.
- Kepert, J. D., J. Schwendike, and H. Ramsay, 2016: Why is the tropical cyclone boundary layer not “well mixed”? *J. Atmos. Sci.*, **73**, 957–973, <https://doi.org/10.1175/JAS-D-15-0216.1>.
- Kieper, M., and H. Jiang, 2012: Predicting tropical cyclone rapid intensification using the 37 GHz ring pattern identified from passive microwave measurements. *Geophys. Res. Lett.*, **39**, L13804, <https://doi.org/10.1029/2012GL052115>.
- Klotz, B. W., and E. W. Uhlhorn, 2014: Improved stepped frequency microwave radiometer tropical cyclone surface winds in heavy precipitation. *J. Atmos. Oceanic Technol.*, **31**, 2392–2408, <https://doi.org/10.1175/JTECH-D-14-00028.1>.
- Lee, C.-Y., and S. S. Chen, 2014: Stable boundary layer and its impact on tropical cyclone structure in a coupled atmosphere-ocean model. *Mon. Wea. Rev.*, **142**, 1927–1944, <https://doi.org/10.1175/MWR-D-13-00122.1>.
- Leighton, H., S. Gopalakrishnan, J. A. Zhang, R. F. Rogers, Z. Zhang, and V. Tallapragada, 2018: Azimuthal distribution of deep convection, environmental factors, and tropical cyclone rapid intensification: A perspective from HWRF ensemble forecasts of Hurricane Edouard (2014). *J. Atmos. Sci.*, **75**, 275–295, <https://doi.org/10.1175/JAS-D-17-0171.1>.
- Li, Q., and Y. Dai, 2020: Revisiting azimuthally asymmetric moist instability in the outer core of sheared tropical cyclones. *Mon. Wea. Rev.*, **148**, 1297–1319, <https://doi.org/10.1175/MWR-D-19-0004.1>.
- Lin, I.-I., C.-C. Wu, K. A. Emanuel, I.-H. Lee, C.-R. Wu, and I.-F. Pun, 2005: The interaction of Supertyphoon Maemi (2003) with a warm ocean eddy. *Mon. Wea. Rev.*, **133**, 2635–2649, <https://doi.org/10.1175/MWR3005.1>.
- , —, I.-F. Pun, and D.-S. Ko, 2008: Upper ocean thermal structure and the western North Pacific category-5 typhoons. Part I: Ocean features and category-5 typhoon’s intensification. *Mon. Wea. Rev.*, **136**, 3288–3306, <https://doi.org/10.1175/2008MWR2277.1>.
- Malkus, J. S., and H. Riehl, 1960: On the dynamics and energy transformations in steady-state hurricanes. *Tellus*, **12**, 1–20, <https://doi.org/10.3402/tellusa.v12i1.9351>.
- Marks, F., and L. K. Shay, 1998: Landfalling tropical cyclones: Forecast problems and associated research opportunities. *Bull. Amer. Meteor. Soc.*, **79**, 305–323, [https://doi.org/10.1175/1520-0477\(1998\)079<0305:LTCFP>2.0.CO;2](https://doi.org/10.1175/1520-0477(1998)079<0305:LTCFP>2.0.CO;2).
- Miyamoto, Y., and D. S. Nolan, 2018: Structural changes preceding rapid intensification in tropical cyclones as shown in a large ensemble of idealized simulations. *J. Atmos. Sci.*, **75**, 555–569, <https://doi.org/10.1175/JAS-D-17-0177.1>.
- Molinari, J., J. Frank, and D. Vollaro, 2013: Convective bursts, downdraft cooling, and boundary layer recovery in a sheared tropical storm. *Mon. Wea. Rev.*, **141**, 1048–1060, <https://doi.org/10.1175/MWR-D-12-00135.1>.
- Nguyen, L. T., R. Rogers, and P. D. Reasor, 2017: Thermodynamic and kinematic influences on precipitation symmetry in sheared tropical cyclones: Bertha and Cristobal (2014). *Mon. Wea. Rev.*, **145**, 4423–4446, <https://doi.org/10.1175/MWR-D-17-0073.1>.
- , —, J. Zawislak, and J. A. Zhang, 2019: Assessing the influence of convective downdrafts and surface enthalpy fluxes on tropical cyclone intensity change in moderate vertical wind shear. *Mon. Wea. Rev.*, **147**, 3519–3534, <https://doi.org/10.1175/MWR-D-18-0461.1>.
- Onderlinde, M. J., and D. S. Nolan, 2017: The tropical cyclone response to changing wind shear using the method of time-varying point-downscaling. *J. Adv. Model. Earth Syst.*, **9**, 908–931, <https://doi.org/10.1002/2016MS000796>.
- Powell, M. D., 1990: Boundary layer structure and dynamics in outer hurricane rainbands. Part II: Downdraft modification and mixed layer recovery. *Mon. Wea. Rev.*, **118**, 918–938, [https://doi.org/10.1175/1520-0493\(1990\)118<0918:BLSADI>2.0.CO;2](https://doi.org/10.1175/1520-0493(1990)118<0918:BLSADI>2.0.CO;2).
- Rappin, E. D., and D. S. Nolan, 2012: The effect of vertical shear orientation on tropical cyclogenesis. *Quart. J. Roy. Meteor. Soc.*, **138**, 1035–1054, <https://doi.org/10.1002/qj.977>.
- Reasor, P. D., and M. D. Eastin, 2012: Rapidly intensifying Hurricane Guillermo (1997). Part II: Resilience in shear. *Mon. Wea. Rev.*, **140**, 425–444, <https://doi.org/10.1175/MWR-D-11-00080.1>.
- , M. T. Montgomery, and L. D. Grasso, 2004: A new look at the problem of tropical cyclones in vertical shear flow: Vortex resiliency. *J. Atmos. Sci.*, **61**, 3–22, [https://doi.org/10.1175/1520-0469\(2004\)061<0003:ANLATP>2.0.CO;2](https://doi.org/10.1175/1520-0469(2004)061<0003:ANLATP>2.0.CO;2).
- , M. D. Eastin, and J. F. Gamache, 2009: Rapidly intensifying Hurricane Guillermo (1997). Part I: Low-wavenumber structure and evolution. *Mon. Wea. Rev.*, **137**, 603–631, <https://doi.org/10.1175/2008MWR2487.1>.

- , R. F. Rogers, and S. Lorsolo, 2013: Environmental flow impacts on tropical cyclone structure diagnosed from airborne Doppler radar composites. *Mon. Wea. Rev.*, **141**, 2949–2969, <https://doi.org/10.1175/MWR-D-12-00334.1>.
- Riemer, M., 2016: Meso- β -scale environment for the stationary band complex of vertically sheared tropical cyclones. *Quart. J. Roy. Meteor. Soc.*, **142**, 2442–2451, <https://doi.org/10.1002/qj.2837>.
- , and M. T. Montgomery, 2011: Simple kinematic models for the environmental interaction of tropical cyclones in vertical wind shear. *Atmos. Chem. Phys.*, **11**, 9395–9414, <https://doi.org/10.5194/acp-11-9395-2011>.
- , —, and M. E. Nicholls, 2010: A new paradigm for intensity modification of tropical cyclones: Thermodynamic impact of vertical wind shear on the inflow layer. *Atmos. Chem. Phys.*, **10**, 3163–3188, <https://doi.org/10.5194/acp-10-3163-2010>.
- , —, and —, 2013: Further examination of the thermodynamic modification of the inflow layer of tropical cyclones by vertical wind shear. *Atmos. Chem. Phys.*, **13**, 327–346, <https://doi.org/10.5194/acp-13-327-2013>.
- Rios-Berrios, R., and R. D. Torn, 2017: Climatological analysis of tropical cyclone intensity changes under moderate vertical wind shear. *Mon. Wea. Rev.*, **145**, 1717–1738, <https://doi.org/10.1175/MWR-D-16-0350.1>.
- , —, and C. A. Davis, 2016a: An ensemble approach to investigate tropical cyclone intensification in sheared environments. Part I: Katia (2011). *J. Atmos. Sci.*, **73**, 71–93, <https://doi.org/10.1175/JAS-D-15-0052.1>.
- , —, and —, 2016b: An ensemble approach to investigate tropical cyclone intensification in sheared environments. Part II: Ophelia (2011). *J. Atmos. Sci.*, **73**, 1555–1575, <https://doi.org/10.1175/JAS-D-15-0245.1>.
- , C. A. Davis, and R. D. Torn, 2018: A hypothesis for the intensification of tropical cyclones under moderate vertical wind shear. *J. Atmos. Sci.*, **75**, 4149–4173, <https://doi.org/10.1175/JAS-D-18-0070.1>.
- Rogers, R., and Coauthors, 2006: The intensity forecasting experiment: A NOAA multiyear field program for improving tropical cyclone intensity forecasts. *Bull. Amer. Meteor. Soc.*, **87**, 1523–1538, <https://doi.org/10.1175/BAMS-87-11-1523>.
- , S. Lorsolo, P. Reasor, J. Gamache, and F. Marks, 2012: Multiscale analysis of tropical cyclone kinematic structure from airborne Doppler radar composites. *Mon. Wea. Rev.*, **140**, 77–99, <https://doi.org/10.1175/MWR-D-10-05075.1>.
- , and Coauthors, 2013a: NOAA's hurricane intensity forecasting experiment: A progress report. *Bull. Amer. Meteor. Soc.*, **94**, 859–882, <https://doi.org/10.1175/BAMS-D-12-00089.1>.
- , P. D. Reasor, and S. Lorsolo, 2013b: Airborne Doppler observations of the inner-core structural differences between intensifying and steady-state tropical cyclones. *Mon. Wea. Rev.*, **141**, 2970–2991, <https://doi.org/10.1175/MWR-D-12-00357.1>.
- , P. Reasor, and J. Zhang, 2015: Multiscale structure and evolution of Hurricane Earl (2010) during rapid intensification. *Mon. Wea. Rev.*, **143**, 536–562, <https://doi.org/10.1175/MWR-D-14-00175.1>.
- , J. Zhang, J. Zawislak, H. Jiang, G. R. Alvey III, E. J. Zipser, and S. N. Stevenson, 2016: Observations of the structure and evolution of Hurricane Edouard (2014) during intensity change. Part II: Kinematic structure and the distribution of deep convection. *Mon. Wea. Rev.*, **144**, 3355–3376, <https://doi.org/10.1175/MWR-D-16-0017.1>.
- Rotunno, R., and K. A. Emanuel, 1987: An air-sea interaction theory for tropical cyclones. Part II: Evolutionary study using a non-hydrostatic axisymmetric numerical model. *J. Atmos. Sci.*, **44**, 542–561, [https://doi.org/10.1175/1520-0469\(1987\)044<0542:AAITFT>2.0.CO;2](https://doi.org/10.1175/1520-0469(1987)044<0542:AAITFT>2.0.CO;2).
- Rudzin, J. E., L. K. Shay, B. Jaimes, and J. K. Brewster, 2017: Upper ocean observations in eastern Caribbean Sea reveal barrier layer within a warm core eddy. *J. Geophys. Res. Oceans*, **122**, 1057–1071, <https://doi.org/10.1002/2016JC012339>.
- , —, and W. E. Johns, 2018: The influence of the barrier layer on SST response during tropical cyclone wind forcing using idealized experiments. *J. Phys. Oceanogr.*, **48**, 1471–1478, <https://doi.org/10.1175/JPO-D-17-0279.1>.
- , —, and B. Jaimes de la Cruz, 2019: The impact of the Amazon–Orinoco River plume on enthalpy flux and air-sea interaction within Caribbean Sea tropical cyclones. *Mon. Wea. Rev.*, **147**, 931–950, <https://doi.org/10.1175/MWR-D-18-0295.1>.
- Ryglicki, D. R., J. H. Cossuth, D. Hodyss, and J. D. Doyle, 2018a: The unexpected rapid intensification of tropical cyclones in moderate vertical wind shear. Part I: Overview and observations. *Mon. Wea. Rev.*, **146**, 3773–3800, <https://doi.org/10.1175/MWR-D-18-0020.1>.
- , J. D. Doyle, Y. Jin, D. Hodyss, and J. H. Cossuth, 2018b: The unexpected rapid intensification of tropical cyclones in moderate vertical wind shear. Part II: Vortex tilt. *Mon. Wea. Rev.*, **146**, 3801–3825, <https://doi.org/10.1175/MWR-D-18-0021.1>.
- , —, D. Hodyss, J. H. Cossuth, Y. Jin, K. C. Viner, and J. M. Schmidt, 2019: The unexpected rapid intensification of tropical cyclones in moderate vertical wind shear. Part III: Outflow–environment interaction. *Mon. Wea. Rev.*, **147**, 2919–2940, <https://doi.org/10.1175/MWR-D-18-0370.1>.
- Shay, L. K., G. J. Goni, and P. G. Black, 2000: Effects of a warm oceanic feature on hurricane Opal. *Mon. Wea. Rev.*, **128**, 1366–1383, [https://doi.org/10.1175/1520-0493\(2000\)128<1366:EOAWOF>2.0.CO;2](https://doi.org/10.1175/1520-0493(2000)128<1366:EOAWOF>2.0.CO;2).
- , and Coauthors, 2011: Airborne ocean surveys of the Loop Current complex from NOAA WP-3D in support of the Deep Water Horizon oil spill. *Monitoring and Modeling the Deepwater Horizon Oil Spill: A Record-Breaking Enterprise*, Geophys. Monogr., Vol. 195, Amer. Geophys. Union, 131–151.
- Stevenson, S. N., K. L. Corbosiero, and J. Molinari, 2014: The convective evolution and rapid intensification of Hurricane Earl (2010). *Mon. Wea. Rev.*, **142**, 4364–4380, <https://doi.org/10.1175/MWR-D-14-00078.1>.
- , —, M. DeMaria, and J. L. Vigh, 2018: A 10-year survey of tropical cyclone inner-core lightning bursts and their relationship to intensity change. *Wea. Forecasting*, **33**, 23–36, <https://doi.org/10.1175/WAF-D-17-0096.1>.
- Tang, B., and K. Emanuel, 2010: Midlevel ventilation's constraint on tropical cyclone intensity. *J. Atmos. Sci.*, **67**, 1817–1830, <https://doi.org/10.1175/2010JAS3318.1>.
- , —, 2012: Sensitivity of tropical cyclone intensity to ventilation in an axisymmetric model. *J. Atmos. Sci.*, **69**, 2394–2413, <https://doi.org/10.1175/JAS-D-11-0232.1>.
- Tao, C., and H. Jiang, 2015: Distributions of shallow to very deep precipitation–convection in rapidly intensifying tropical cyclones. *J. Climate*, **28**, 8791–8824, <https://doi.org/10.1175/JCLI-D-14-00448.1>.
- , —, and J. Zawislak, 2017: The relative importance of stratiform and convective rainfall in rapidly intensifying tropical cyclones. *Mon. Wea. Rev.*, **145**, 795–809, <https://doi.org/10.1175/MWR-D-16-0316.1>.

- Tao, D., and F. Zhang, 2014: Effect of environmental shear, sea-surface temperature and ambient moisture on the formation and predictability of tropical cyclones: An ensemble-mean perspective. *J. Adv. Model. Earth Syst.*, **6**, 384–404, <https://doi.org/10.1002/2014MS000314>.
- Wadler, J. B., R. F. Rogers, and P. D. Reasor, 2018a: The relationship between spatial variations in the structure of convective bursts and tropical cyclone intensification as determined by airborne Doppler radar. *Mon. Wea. Rev.*, **146**, 761–780, <https://doi.org/10.1175/MWR-D-17-0213.1>.
- , J. A. Zhang, B. Jaimes, and L. K. Shay, 2018b: Downdrafts and the evolution of boundary layer thermodynamics in Hurricane Earl (2010) before and during rapid intensification. *Mon. Wea. Rev.*, **146**, 3545–3565, <https://doi.org/10.1175/MWR-D-18-0090.1>.
- Walker, N., S. Myint, A. Babin, and A. Haag, 2003: Advances in satellite radiometry for the surveillance of surface temperatures, ocean eddies and upwelling processes in the Gulf of Mexico using GOES-8 measurements during summer. *Geophys. Res. Lett.*, **30**, 1854, <https://doi.org/10.1029/2003GL017555>.
- Wang, Y., J. D. Kepert, and G. J. Holland, 2001: The effect of sea spray evaporation on tropical cyclone boundary layer structure and intensity. *Mon. Wea. Rev.*, **129**, 2481–2500, [https://doi.org/10.1175/1520-0493\(2001\)129<2481:TEOSSE>2.0.CO;2](https://doi.org/10.1175/1520-0493(2001)129<2481:TEOSSE>2.0.CO;2).
- Willoughby, H. E., and M. B. Chelmow, 1982: Objective determination of hurricane tracks from aircraft observations. *Mon. Wea. Rev.*, **110**, 1298–1305, [https://doi.org/10.1175/1520-0493\(1982\)110<1298:ODOHTF>2.0.CO;2](https://doi.org/10.1175/1520-0493(1982)110<1298:ODOHTF>2.0.CO;2).
- , F. D. Marks Jr., and R. J. Feinberg, 1984: Stationary and moving convective bands in hurricanes. *J. Atmos. Sci.*, **41**, 3189–3211, [https://doi.org/10.1175/1520-0469\(1984\)041<3189:SACB>2.0.CO;2](https://doi.org/10.1175/1520-0469(1984)041<3189:SACB>2.0.CO;2).
- Wroe, D. R., and G. M. Barnes, 2003: Inflow layer energetics of Hurricane Bonnie (1998) near landfall. *Mon. Wea. Rev.*, **131**, 1600–1612, <https://doi.org/10.1175//2547.1>.
- Yablonsky, R. M., and I. Ginis, 2013: Impact of a warm ocean eddy's circulation on hurricane-induced sea surface cooling with implications for hurricane intensity. *Mon. Wea. Rev.*, **141**, 997–1021, <https://doi.org/10.1175/MWR-D-12-00248.1>.
- Zagrodnik, J. P., and H. Jiang, 2014: Rainfall, convection, and latent heating distributions in rapidly intensifying tropical cyclones. *J. Atmos. Sci.*, **71**, 2789–2809, <https://doi.org/10.1175/JAS-D-13-0314.1>.
- Zavala-Hidalgo, J., S. L. Morey, and J. J. O'Brien, 2003: Cyclonic eddies northeast of the Campeche Bank from altimetry data. *J. Phys. Oceanogr.*, **33**, 623–629, [https://doi.org/10.1175/1520-0485\(2003\)033<0623:CENOTC>2.0.CO;2](https://doi.org/10.1175/1520-0485(2003)033<0623:CENOTC>2.0.CO;2).
- Zawislak, J., H. Jiang, G. Alvey, E. Zipser, R. Rogers, J. Zhang, and S. Stevenson, 2016: Observations of the structure and evolution of Hurricane Edouard (2014) during intensity change. Part I: Relationship between the thermodynamic structure and precipitation. *Mon. Wea. Rev.*, **144**, 3333–3354, <https://doi.org/10.1175/MWR-D-16-0018.1>.
- Zhang, F., and D. Tao, 2013: Effects of vertical wind shear on the predictability of tropical cyclones. *J. Atmos. Sci.*, **70**, 975–983, <https://doi.org/10.1175/JAS-D-12-0133.1>.
- Zhang, J. A., and R. F. Rogers, 2019: Effects of parameterized boundary layer structure on hurricane rapid intensification in shear. *Mon. Wea. Rev.*, **147**, 853–871, <https://doi.org/10.1175/MWR-D-18-0010.1>.
- , P. G. Black, J. R. French, and W. M. Drennan, 2008: First direct measurements of enthalpy flux in the hurricane boundary layer: The CBLAST results. *Geophys. Res. Lett.*, **35**, L14813, <https://doi.org/10.1029/2008GL034374>.
- , R. F. Rogers, D. S. Nolan, and F. D. Marks, 2011: On the characteristic height scales of the hurricane boundary layer. *Mon. Wea. Rev.*, **139**, 2523–2535, <https://doi.org/10.1175/MWR-D-10-05017.1>.
- , R. Rogers, P. Reasor, E. Uhlhorn, and F. Marks, 2013: Asymmetric hurricane boundary layer structure from dropsonde composites in relation to the environmental vertical wind shear. *Mon. Wea. Rev.*, **141**, 3968–3984, <https://doi.org/10.1175/MWR-D-12-00335.1>.
- , J. J. Cione, E. A. Kalina, E. W. Uhlhorn, T. Hock, and J. A. Smith, 2017: Observations of infrared sea surface temperature and air-sea interaction in Hurricane Edouard (2014) using GPS dropsondes. *J. Atmos. Oceanic Technol.*, **34**, 1333–1349, <https://doi.org/10.1175/JTECH-D-16-0211.1>.